JGR Oceans

RESEARCH ARTICLE
10.1029/2021JC017938

On the Groupiness and Intermittency of Oceanic Whitecaps

M. P. Malila[1,2,3], J. Thomson[3,4], Ø. Breivik[1,2], A. Benetazzo[5], B. Scanlon[6], and B. Ward[6]

[1]Norwegian Meteorological Institute, Bergen, Norway, [2]Geophysical Institute, University of Bergen, Bergen, Norway, [3]Department of Civil and Environmental Engineering, University of Washington, Seattle, WA, USA, [4]Applied Physics Laboratory, University of Washington, Seattle, WA, USA, [5]Institute of Marine Sciences (ISMAR), National Research Council (CNR), Venice, Italy, [6]AirSea Laboratory, Centre for Ocean Research and Exploration, Ryan Institute, National University of Ireland, Galway, Ireland

Abstract The enhancement of wave breaking activity during wave group passage is investigated using coherent field observations of the instantaneous sea surface elevation and whitecap coverage from platform-based stereo video measurements in the central North Sea. Passing wave groups are shown to be associated with a two to threefold enhancement in the probability distribution of total whitecap coverage W whereas the enhancement of active whitecap coverage W_A is approximately fivefold. Breaking time scales and intermittency characteristics are also investigated with the inclusion of a secondary data set of W and W_A observations collected during a research cruise in the North Pacific. The time scale analysis suggests a universal periodicity in wave breaking activity within a representative sea-surface area encompassing approximately one dominant wave crest. The breaking periodicity is shown to be closely linked to the peak period of the dominant wave components, suggesting that long-wave modulation of wave breaking is a predominant mechanism controlling the intermittency of wave breaking across scales.

Plain Language Summary In the open ocean, wind waves of similar wavelength, period and direction combine to form wave groups, also known as sets to surfers and other beachgoers. In deep water, the individual waves in groups travel twice as fast as the groups themselves, and momentarily grow in height and steepness in the wave group center, making them theoretically more likely to break. We show, using field observations of wave breaking taken with digital video cameras, that waves in deep water are up to five times more likely to break in large wave groups than during lulls in the wave field. We also show that the large, dominant wave groups regularly initiate wave breaking at a wide range of scales. Our findings can be used to produce more accurate predictions of when individual waves will break, an active and relatively poorly understood area of current wave research.

Key Points:

- Wave breaking activity and extent is significantly enhanced in wave groups
- The periodicity of the oceanic whitecap coverage is closely linked to the periodicity of dominant wave components
- The intermittency characteristics of whitecap coverage approximately follow similarity scaling laws of other general stochastic processes

Correspondence to:
M. P. Malila,
mikapm@met.no

Citation:
Malila, M. P., Thomson, J., Breivik, Ø., Benetazzo, A., Scanlon, B., & Ward, B. (2022). On the groupiness and intermittency of oceanic whitecaps. *Journal of Geophysical Research: Oceans*, *127*, e2021JC017938. https://doi.org/10.1029/2021JC017938

Received 25 AUG 2021
Accepted 6 JAN 2022

Author Contributions:
Conceptualization: M. P. Malila, J. Thomson, Ø. Breivik
Data curation: M. P. Malila
Formal analysis: M. P. Malila
Funding acquisition: Ø. Breivik, B. Ward
Investigation: M. P. Malila
Methodology: M. P. Malila, A. Benetazzo, B. Scanlon
Resources: J. Thomson, B. Scanlon, B. Ward
Software: M. P. Malila, A. Benetazzo
Supervision: J. Thomson, Ø. Breivik
Validation: M. P. Malila
Visualization: M. P. Malila
Writing – original draft: M. P. Malila
Writing – review & editing: J. Thomson, Ø. Breivik, A. Benetazzo, B. Scanlon, B. Ward

1. Introduction

The breaking in deep water of wind-generated ocean surface waves is an intermittent process, scattered unevenly in space and time and occurring over a variety of scales. Breaking waves dissipate wave energy as turbulence and entrain air in bubbles just below the surface (Thorpe, 1982). Turbulent dissipation rates immediately beneath breaking waves are orders of magnitude above values encountered in non-breaking regions (Agrawal et al., 1992; Derakhti, Thomson, & Kirby, 2020; Gemmrich & Farmer, 1999; Sutherland & Melville, 2015; Terray et al., 1996; Thomson et al., 2016). The bubbles generated during wave breaking are a dominant mechanism driving air-sea gas exchange (Melville, 1996; Zappa et al., 2007). In engineering applications, large-scale breaking can cause critical loading on offshore structures (Chella et al., 2012). The energy dissipation due to wave breaking limits wave growth, and balances the energy input by wind and wave-wave energy transfer in the spectral equilibrium range (Komen et al., 1994; Phillips, 1985). The steep forward faces of breaking waves also induce airflow separation, which may significantly enhance the local momentum transfer between air and sea (Banner & Melville, 1976; Buckley & Veron, 2016; Reul et al., 2008). Wave breaking also affects the roughness and emissivity of the sea surface, and is therefore important to account for in remote sensing applications (Anguelova & Webster, 2006; Monahan & O'Muircheartaigh, 1986; Salisbury et al., 2013).

Considerable effort has been directed in recent decades into formulating a framework that successfully describes and predicts the evolution of wave crests toward the onset of breaking (Babanin et al., 2007; Banner et al., 2000; Banner & Peirson, 2007; Barthelemy et al., 2018; Derakhti & Kirby, 2016; Derakhti, Kirby, et al., 2020; Saket et al., 2017; Song & Banner, 2002). The onset is closely linked to wave geometry, which for simple plane waves

is described by the wave steepness H/λ, where H is the wave height and λ is the wavelength. The classical Stokes irrotational water wave profile (Stokes, 1880) can be shown to be unable to maintain its shape, leading to an uncontrolled collapse of the surface, when $H/\lambda > 1/7$, or equivalently, $ak > 0.443$, where $a = H/2$ is the wave amplitude and $k = 2\pi/\lambda$ is the wavenumber (Michell, 1893). Kinematically, the collapse of the wave profile during breaking is due to the particle velocity at the wave crest exceeding the phase speed c of the wave, whereas in a dynamic sense breaking occurs when the downward acceleration of the water surface on the forward face of a wave surpasses a limiting threshold (Babanin, 2011; Perlin et al., 2013). Recently, Barthelemy et al. (2018) introduced a novel dynamic breaking threshold formalism based on the flux convergence of mechanical wave group energy focused on the crest region of the highest wave of a group.

The focusing of wave components, whether as a result of linear superposition or nonlinear interactions, related to the group structure of directional wave fields has long been thought to influence the onset of wave breaking in deep water. Early observations by Donelan et al. (1972) and Holthuijsen and Herbers (1986) reported recurring breaking patterns at periods linked to the periodicity of the dominant wave field, with breaking apparently occurring preferentially near the central apex of the wave group envelope. Similarly, wave group-related periodic recurrence in wave breaking was found by Smith et al. (1996) in an analysis of "sea spikes" in grazing-angle S-band marine radar records. Terrill and Melville (1997) likewise observed low-frequency modulations in near-surface oceanic sound speed, which they attributed to bubble entrainment due to large-scale breaking occurring at wave-group time scales.

In general, the characteristic steepness of the long, dominant wave components in the open ocean is on the order of $ak_p \approx 0.1$, where k_p is the wavenumber at the peak of the wave spectrum—significantly lower than the critical steepness of $ak \approx 0.443$. Therefore, group focusing mechanisms are quite unlikely to cause their bulk steepness to exceed the critical breaking steepness (Babanin et al., 2011; Holthuijsen & Herbers, 1986; Schwendeman & Thomson, 2017). However, regardless of the underlying focusing mechanism, the group-induced variations in amplitude and steepness experienced by the dominant waves affect the stretching and compression of the shorter, wind-forced wave components in the spectral equilibrium range that ride on the backs of long waves. These modulations affect the breaking probability of the short waves thanks to their higher intrinsic steepness (Guimaraes, 2018). Theoretically, the effect of long wave motions on the short wave steepness can be explained by the straining of the long-wave orbital motions against the excess momentum flux due the short waves, also known as the wave radiation stress (Longuet-Higgins & Stewart, 1960, 1964). Conversely, the long-wave modulations of the breaking characteristics of the short waves have also been shown to impact the growth rate of the long waves due to changes in the form drag over the wave field induced by air flow separation in the breaking regions (Donelan et al., 2010; Kudryavtsev & Chapron, 2016).

Dulov et al. (2002, 2021) investigated the impact of long-wave modulations on the breaking characteristics of short waves using a combination of optical video imagery for breaker detection and an array of wave staffs for measuring the instantaneous sea-surface elevation within the camera footprint. They found strong modulation of the phase and amplitude of the instantaneous *whitecap coverage*, W, by dominant waves, with short-wave breaking most likely to occur at the crests of the long waves. Similarly, Yurovsky et al. (2017) compared the instantaneous W to the instantaneous sea-surface elevation estimated from synchronous K_a-band Doppler radar and optical video recordings, and found that high values of W, indicative of active, large scale wave breaking, coincided with the passage of large wave groups. The group-enhanced breaking was found to be significant in young, growing sea states with marked group structure, while the breaking in old, decaying sea states was generally smaller in scale and more random in character, with a smaller degree of coincidence with the group structure of the wave field. In another recent study, Schwendeman and Thomson (2017) used high-resolution sea surface reconstructions from stereo video measurements coupled with conventional whitecap identification methods to verify the validity of the Stokes limiting wave profile in the crest regions of breaking directional waves.

Inspired by the approaches of Dulov et al. (2002), Yurovsky et al. (2017), and Dulov et al. (2021), the current study investigates the modulation of wave breaking by dominant wave groups in terms of the time variability of the whitecap coverage W. We employ coherent (i.e., simultaneous and co-located) observations of W and the sea surface elevation, acquired with an optical stereo video camera system installed on a platform in the North Sea, to study the coincidence of elevated wave breaking activity and wave group passage. We also analyze the temporal intermittency and clustering tendencies of the whitecap coverage with the *telegraph approximation* (TA), a methodology that isolates the time variability of a time series from its amplitude variations. The TA formalism has

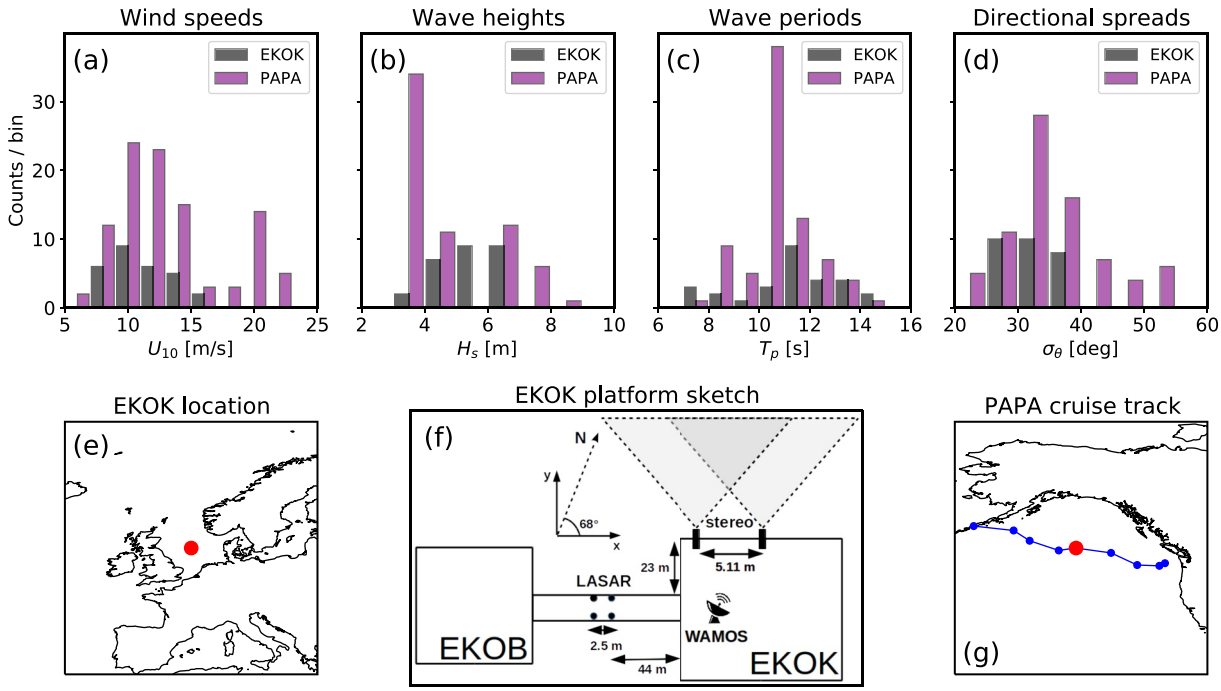

Figure 1. (a)–(d) Histograms summarizing the wind and wave conditions during the acquisition periods of the EKOK and PAPA data sets. The bin heights represent the number of observational records per bin in each data set. (e) The location of the Ekofisk platform (EKOK) at approximately (56.5°N, 003.2°E). (f) Sketch of the Ekofisk K and B platforms, showing the approximate locations of the stereo video cameras, laser altimeter array (LASAR) and WAMOS radar. (g) The cruise track of the December 2019 North Pacific cruise (PAPA) on R/V Sikuliaq. The location of Ocean Station P (50°N, 145°W) is marked with a red dot.

previously been used to uncover similarity structures in other intermittent stochastic processes such as turbulent velocity and temperature fluctuations (Cava et al., 2012; Huang et al., 2021; Sreenivasan & Bershadskii, 2006). However, to our knowledge this is the first application of the TA to the study of the intermittency of wave breaking. For the investigation of the time scales of breaking, we introduce an additional field data set of W measurements collected during a recent cruise in the North Pacific.

The remainder of this text is structured as follows. The field data sets are introduced in Section 2. The data processing methods are described in Section 3 and the analysis methods in Section 4. Our results are presented and discussed in Section 5 and concluding remarks are delivered in Section 6.

2. Data

2.1. North Sea Stereo Video Measurements

A dual camera stereo video system was installed in 2017 on the Ekofisk K platform, located in the central North Sea within the extensive Ekofisk oil and gas field. The stereo video footprint faces open waters toward the northwest (see Figures 1e and 1f), and the closest platforms to the south are ∼2 km away. The stereo video system consists of two PointGrey Blackfly GiGE CCD digital cameras fitted with Edmund Optics 12 mm fixed-focal length lenses. The cameras are separated by a 5.11 m baseline distance, and sit approximately 28 m above mean sea level. The cameras are oriented with parallel lines of sight and oblique viewing angles approximately 70° from nadir. The camera viewing angles were set by aligning the fields of view so that the horizon lies just out of frame above the upper edge of the image frames. This maximizes the sea surface area covered by the stereo images while avoiding potentially abrupt pixel intensity gradients at the horizon line which may negatively interfere with the cameras' automatic exposure adjustment.

The northwest-facing orientation of the stereo video system was chosen to ensure exposure to the longest unobstructed fetch associated with weather systems approaching from the north, as well as to minimize unwanted sun glare in the stereo video images. Minimizing sun glare is important from an image processing perspective, as the stereo reconstruction of the wave field assumes a near-Lambertian sea surface for which the reflecting properties

are independent of viewing angle (Jähne et al., 1994). The stereo video image acquisition is controlled using an Arduino Uno microcontroller, which is programed to synchronize the hardware triggering of the cameras and control the frame rate. All of the stereo video sequences analyzed in this study were obtained at a frame rate of five frames per second (fps) and at a resolution of five megapixels (2,048 × 2,448 pixels).

In this study, the images acquired by the stereo cameras will be used to both reconstruct the sea surface elevation at high temporal and spatial resolution (see Section 3.1) as well as to estimate the fractional whitecap coverage W (see Section 3.2). The Ekofisk stereo video data set (hereafter EKOK) consists of 28 20-min stereo video sequences spread over five separate days during the 2019–2020 winter and spring season. Wind speeds were measured on the Ekofisk L platform 2.3 km south of the stereo camera location with a Vaisala WMT703 sonic anemometer located at 102.3 m height above mean sea level. Due to the high elevation of the wind anemometer, the wind speeds at Ekofisk L were converted to 10-m wind speed assuming neutral atmospheric stratification using the power-law approximation

$$U_{10} = U_z(10/H)^{\alpha}, \tag{1}$$

where U_z is the wind measurement observed at height $H = 102.3$ m, and $\alpha = 0.06$. The wind profile approximation in Equation 1 applied to oil platform-based anemometer data in the North Sea was found to best correspond to measured radiosonde wind profiles by Furevik and Haakenstad (2012), as well as more recently to microwave satellite wind speeds by Manaster et al. (2019). Hereafter, all references to U_{10} implicitly mean the equivalent neutral wind. The environmental conditions encountered during the stereo video acquisition periods are summarized in Figure 1, with significant wave height and peak period, H_s and T_p, estimated from the stereo video wave field reconstructions. Due to the limited field of view of the stereo video footprint, the directional spread σ_θ is estimated from two-dimensional spectra obtained from an X-band marine radar using the wave monitoring system WAMOS (Reichert et al., 1999) situated on the helideck of the EKOK platform (at ∼49 m above mean sea level). See also Section 3.1 for a validation of the stereo video wave spectra against the WAMOS product and a nearby laser altimeter array located on a footbridge connecting the EKOK platform to the nearby B platform (see Figure 1f). Additional details of the degree of groupiness of the wave field (group lengths, spectral bandwidth, and directional spread) encountered in the EKOK data set are presented in Section 5.1.

2.2. North Pacific Cruise Data

We supplement the North Sea stereo video measurements with single-camera whitecap coverage estimates acquired during a research cruise onboard the R/V Sikuliaq in the North Pacific Ocean in December 2019. We hereafter refer to this data set with the abbreviation PAPA, after Ocean Station P ("Papa")—an oceanographic observation site in the mid-North Pacific visited during the cruise. The PAPA cruise was a 2.5-week field experiment dedicated to measuring environmental parameters driving the physics of air-sea interactions such as wave breaking and bubble dynamics.

The digital camera setup on the PAPA experiment was identical to the one described in Schwendeman and Thomson (2015a) and analyzed in Schwendeman and Thomson (2015b), and will therefore only be briefly introduced here. Two Point Grey Flea2 digital camera equipped with 2.8 mm focal-length wide angle lenses were attached to the port and starboard railings on the bridge deck of the ship at approximately 16 m height above the water level. Video recordings at frame rates between 5 and 7.5 fps and 1,288 × 964 pixels resolution were acquired at times when the vessel was held stationary due to other sampling activity such as buoy deployments and recoveries or vertical water profiling casts. Only one of the cameras could be operated at a time, and the choice of which camera to operate was generally motivated by the ship's heading (to minimize sky reflections or direct sunlight) and local wind direction (to avoid droplet accumulation on the recording camera lens in the presence of rain or sea spray). The length of the video recordings varied between approximately 5 and 60 min, but only continuous recordings with a minimum length of 10 min were used here for further analysis. Likewise, continuous records longer than 20 min were split into shorter sequences between 10 and 20 min in length.

Wind speeds were measured underway from a sonic anemometer mounted on the ship's bow mast at ∼16 m height. The 16-m wind speeds were converted to neutrally stratified 10-m estimates using the COARE algorithm, a standard procedure for low-elevation, buoy and ship-based wind speed conversion in the marine atmospheric boundary layer (Fairall et al., 2003). The wave field was continuously observed with freely floating, retrievable

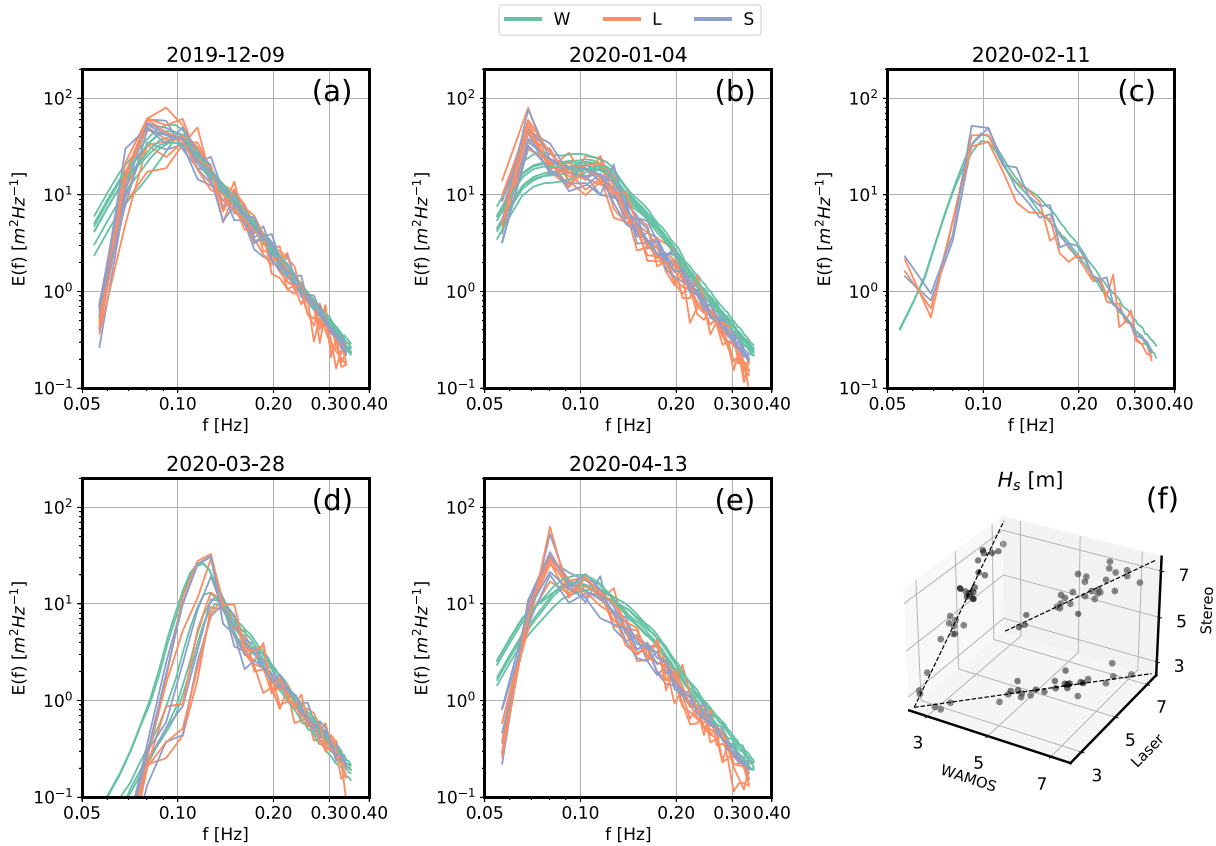

Figure 2. (a)–(e) Comparison of scalar wave spectra from the WAMOS radar (*W*), laser altimeter array (*L*) and stereo video reconstructions (*S*) during the EKOK observational records. (f) Comparison of H_s estimates inferred from the respective spectra.

SWIFT wave buoys (Thomson, 2012), which provided measurements of wave field parameters, such as wave height and period. The buoy locations did not, however, coincide with the footprints covered by the video cameras. See Figure 1 for a synopsis of the sea state conditions encountered during the video acquisitions on the PAPA cruise. Details of the groupiness of the wave field in the PAPA data set are given in Section 5.1.

3. Data Processing Methods

3.1. Stereo Video Reconstruction

The EKOK stereo video image pairs were used to reconstruct the instantaneous sea-surface topography with the open-source stereo wave processing software "Waves Acquisition Stereo System" (WASS), see Benetazzo (2006), Benetazzo et al. (2012), and Bergamasco et al. (2017). WASS automates the processing steps required to perform the extrinsic calibration, feature matching, and triangulation, producing three-dimensional point clouds of the instantaneous sea surface elevation, which we later interpolated onto regular 2-D x, y grids with 50×50 cm^2 grid size. The intrinsic calibration is not automated and was performed manually on the platform on 7 August 2019, prior to the acquisition and processing of the images.

In Figure 2, we compare scalar wave energy frequency spectra $E(f)$ estimated from virtual wave staffs within 20-min sequential stereo video grids against spectra from a nearby 5-Hz laser altimeter array (Magnusson & Donelan, 2013) and the WAMOS radar. All spectra are truncated at a low frequency of 0.05 Hz and a high-frequency cutoff of 0.35 Hz in order to cover the fairly limited frequency range of the WAMOS radar. The spectral shapes from the stereo video and the laser altimeters show good agreement, while the WAMOS spectra—obtained by integrating the frequency-directional spectra over all directions—are generally smoother and display less pronounced peaks, especially in the low-frequency swell range. However, the estimates of the significant wave height

Table 1
Stereo Video and Image Grid Characteristics in the EKOK and PAPA Data Sets

Data set	Grid type	Grid variable	Spatial resolution [m]	Frame rate [fps]	Area [m^2]
EKOK	Stereo video	η [m]	0.5	5	4,020
EKOK	Image	Pixel intensity	0.5	5	4,020
PAPA	Image	Pixel intensity	0.8	5–7.5	6,504 (5,416, 7,964)

Note. The PAPA grid area reported is the median area, and the maximum and minimum areas are in parentheses.

$H_s = 4\sqrt{m_0}$, inferred from the zeroth-order spectral moments m_0 and compared in Figure 2f, are quite consistent across all instruments.

3.2. Whitecap Thresholding

In this section, we describe our process for estimating, via pixel brightness thresholding operations, the fractional whitecap coverage from the optical imagery in EKOK and PAPA field data sets. Hereafter, we will refer to two separate quantities related to the whitecap coverage, namely the total whitecap coverage W, which quantifies the full fractional coverage of whitecap-related foam present on the sea surface at any given time, and the active whitecap coverage W_A, in which only the actively breaking contribution of the whitecap coverage is considered. Moreover, we use the variable names W and W_A to refer to the instantaneous, frame-wise whitecap coverage, whereas $\overline{W}$ and $\overline{W}_A$ refer to time-averaged quantities.

Prior to whitecap thresholding, the digital video frames from the EKOK and PAPA data sets were geo-rectified into earth-referenced projections and gridded onto regular x, y grids using Delaunay triangulation and bi-linear interpolation. Since the EKOK data set includes double frames for each time step while only one frame is required for whitecap thresholding, only frames from the left camera were used. The EKOK frames were geo-rectified using the camera pose estimated by the extrinsic calibration of the stereo video analysis, and interpolated onto grids of the same shape as the sea-surface reconstructions. The ship-based PAPA video frames were stabilized and geo-rectified using the horizon-tracking algorithm of Schwendeman and Thomson (2015a) and interpolated onto grids with 80 cm grid cell side length. Due to the rolling motion of the ship, the PAPA grid sizes display small variations depending on the instantaneous angle of view. In general, the PAPA image grids cover a somewhat larger footprint than the EKOK grids because of the wider angle lenses used. We also performed the analysis presented in this study on reduced (i.e., cropped) grid sizes for the PAPA data set, but found no significant impact on the results, supporting similar findings reported by Schwendeman and Thomson (2015b). Table 1 summarizes the grid characteristics in the two data sets.

3.2.1. Total Whitecap Coverage W

We estimated the fractional whitecap coverage W from the image grids in both data sets following the pixel threshold-based approach of Kleiss and Melville (2011). By examining the shapes of the cumulative pixel intensity histograms of several sequential grayscale image grids, this methodology identifies a pixel intensity value above which the pixels likely represent foam from either actively breaking waves or decaying whitecaps. The thresholding operation results in binary image grids, and the instantaneous value of W is calculated as the fraction of pixels whose value exceeds the threshold within each grid. Due to the potential presence of other bright features in the images apart from whitecap foam, such as sun glints or rain droplets, we performed a manual inspection of the thresholded image grids to verify that the thresholding mainly isolates the foam while largely ignoring other bright features. In some cases in the PAPA image data set (where the camera exposure was controlled manually), we manually varied the pixel threshold to optimally isolate the foam. Image grid sequences with extensive amounts of sky reflections or droplet accumulation on the camera lenses were discarded.

3.2.2. Active Whitecap Coverage W_A

The thresholding approach outlined above produces estimates of the total whitecap coverage W within the camera footprint, including the residual decaying foam of previously broken waves. To estimate the fractional whitecap coverage due to actively breaking waves, W_A, we followed the approach of Schwendeman and Thomson (2015b),

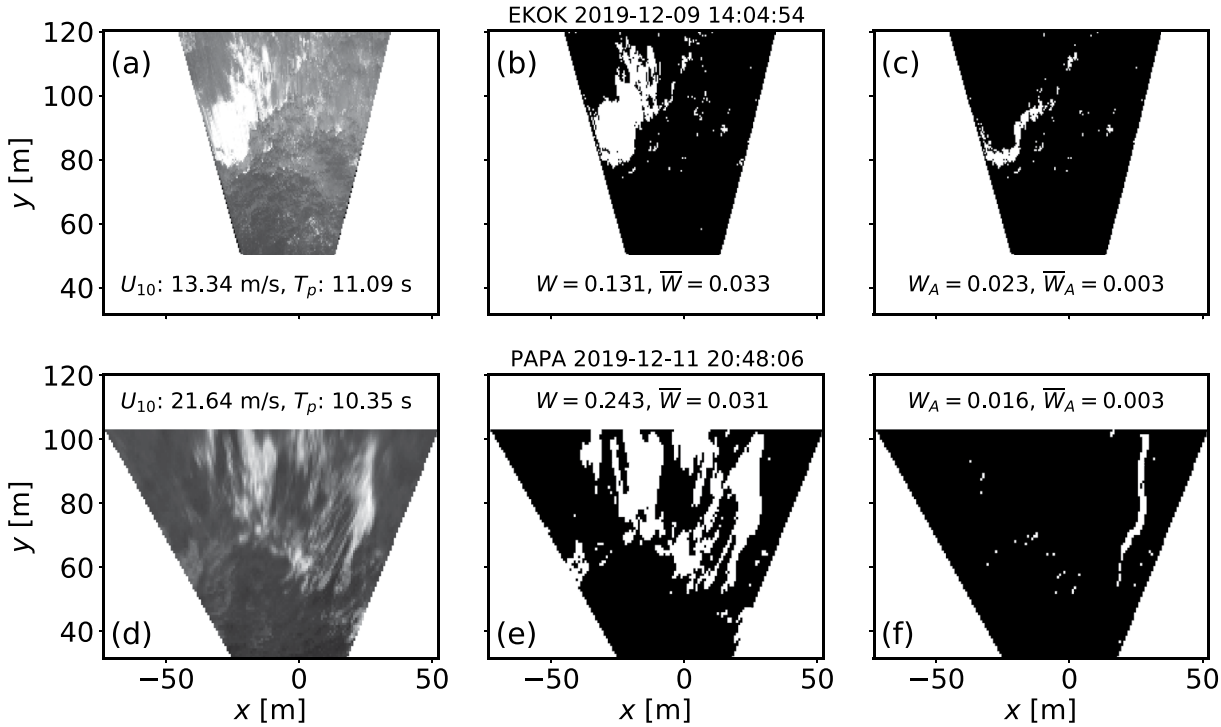

Figure 3. Sample image grid snapshots from the EKOK (upper row) and PAPA (lower row) data sets, displaying the differences between whitecap foam classification for total whitecap coverage W and actively breaking whitecap coverage W_A. Panels (a) and (d) show geo-rectified image grids in which each pixel (i.e., grid cell) can take on integer values between 0 (black) and 255 (white). The prevailing wind speed U_{10} and peak wave period T_p are annotated under/above the original image grids in (a) and (d). Panels (b) and (e) show the resulting binary grids of the thresholding process of Kleiss and Melville (2011) applied on the original image grids, where the pixels representing whitecap-related foam (white pixels with value 1) have been isolated from the background sea surface (black pixels with value 0). Panels (c) and (f) show the estimated actively breaking foam fraction, determined following the approach of Schwendeman and Thomson (2015b). The instantaneous values of W and W_A for each example frame, as well as the respective record-mean values $\overline{W}$ and $\overline{W}_A$, are annotated under/above the respective binary image grids.

in which the binary pixels of a thresholded image grid are assumed to be part of an actively breaking wave crest the first time the pixel values change from 0 to 1 within a short time period. The assumption is that the pixels remain "flipped" until the remnant foam patch has dissipated. In our W_A analysis, we set the time lag for tracking the pixel value changes to 10 s, which in most of our field data corresponds approximately to the period of the dominant waves (see Figure 1c). As the example in Figure 3 shows, this method of W_A classification only isolates the leading crests of breaking waves, potentially leading to lower values of time averaged W_A compared to observations based on different classification criteria, for example, dynamically motivated filtering algorithms (Mironov & Dulov, 2008) or manually selected image features (Scanlon & Ward, 2013). However, the W_A estimates produced by the method of Schwendeman and Thomson (2015b) effectively pinpoint the location and time of breaking initiation, and are therefore well-suited to the purpose of this study, namely the analysis of the group-enhancement of breaking activity (see Section 5.2) and breaking intermittency (see Section 5.3).

4. Analysis Methods

The analysis conducted in this study can be divided into two main parts. First, we investigate the wave group-enhancement of the whitecap coverage from the coherent sea surface height-whitecapping information in the EKOK data set only. The methods for identifying wave groups from the stereo video reconstructions are described in Section 4.1. The second part of the analysis concerns the intermittency and clustering of the whitecap coverage. This part only requires time series of the whitecap coverage, and is therefore performed on both the EKOK and PAPA data sets. The intermittency analysis methodology is described in Section 4.2.

4.1. Wave Group Detection

The tendency of dominant waves to occur in distinct groups of successive high waves is enhanced when the wave energy frequency spectrum $E(f)$ is narrow (Goda, 1970; Longuet-Higgins, 1984). In the canonical JONSWAP parameterization of developing wave spectra (Hasselmann et al., 1973), the peakedness of the wave spectrum is modeled with a peak enhancement factor that has been shown to depend strongly on wave age, with young, growing seas typically exhibiting relatively narrow, peaked spectra that correspond to pronounced wave field groupiness (Donelan et al., 1985). The spectral width is commonly estimated with the bandwidth parameter of Longuet-Higgins (1975),

$$\nu = \sqrt{\frac{m_2 m_0}{m_1^2} - 1}, \tag{2}$$

where m_n is the n-th spectral moment,

$$m_n = \int_0^\infty f^n E(f)\,\mathrm{d}f. \tag{3}$$

However, due to its dependence on the second-order spectral moment m_2, the value of the ν parameter is sensitive to the high-frequency spectral cutoff. For this reason, a more robust bandwidth measure can be composed from the spectral peakedness parameter of Goda (1970),

$$Q_p = \frac{2}{m_0^2} \int_0^\infty f E^2(f)\,\mathrm{d}f. \tag{4}$$

Following Janssen and Bidlot (2009), the spectral bandwidth in the spectral peak region can be estimated with the inverse peakedness parameter Q_p^{-1}.

Due to the dispersive nature of waves in deep water, individual dominant wave components advance through wave groups at the phase speed $c = 2c_g$, where c_g is the group speed of wave energy propagation, undergoing modulations of their amplitude and steepness underway. This type of dispersive wave energy focusing is primarily a *linear* effect caused by additive superpositions of wave components with different wavelengths and frequencies. Linear superposition of wave components may also occur due to the directional focusing of wave trains traveling in crossing directions. Another measure of the spectral width that is of importance to the group structure of the wave field is therefore the directional spread σ_θ of the wave energy distribution. The directional spread can be inferred from the distribution of directional components in the frequency-direction wave spectrum $E(f, \theta)$. However, in practice, the directional spread of measured wave spectra is often calculated from the first two-to-four Fourier coefficients of the directional distribution, since these coefficients are readily estimated from the cross spectra of the horizontal and vertical displacements of for example, drifting wave buoys (Herbers et al., 2012; Kuik et al., 1988).

Under certain conditions, wave groups are also subject to a type of *nonlinear* evolution known as modulational instability, during which the wave spectrum undergoes nonlinear transformations which can lead to pulse-like wave groups with potentially extremely high amplitude and steepness (Benjamin & Feir, 1967). Modulational instability has been shown to produce large-amplitude rogue and breaking waves in laboratory and numerical experiments (Dysthe et al., 2008), but its significance in the real open ocean is a topic of ongoing debate due to the strict assumptions of spectral narrowness in both frequency and directional spread required for the instability to take effect (Adcock et al., 2011; Fedele et al., 2016). Janssen and Bidlot (2009) introduced the parameter

$$R = \frac{\sigma_\theta^2}{2(Q_p^{-1})^2} \tag{5}$$

to quantify the joint contributions of directional spread and frequency bandwidth on the susceptibility of a directional sea state to modulational instability. Within the range $0 < R < 1$, Janssen and Bidlot (2009) considered the wave field to be in a focusing regime in which wave field nonlinearity is enhanced, whereas $R \geq 1$ implies a defocussing regime in which nonlinear interactions are suppressed by directional dispersion.

In this study we define wave groups as periods of elevated wave energy within a wave record. Focusing here solely on the EKOK data set, the wave group structure recovered from the stereo video data is directly compared to the coherent whitecap coverage within the same area of the sea surface. In order to isolate groups formed by the dominant waves, we perform a spatial filtering of the EKOK stereo video sea surface reconstructions by averaging each instantaneous elevation grid over a centralized square area whose side length equals one-eighth of the peak wavelength L_p, estimated with the linear dispersion relation from the peak wave period T_p of the point-wise scalar wave energy spectra of the virtual wave staffs (see Section 2.1). This creates the equivalent of a low-pass filtered sea surface elevation time series $\bar{\eta}(t)$, formally defined as

$$\bar{\eta}(t) = \frac{1}{N_x N_y} \sum_{i=1}^{N_x} \sum_{j=1}^{N_y} \eta_{ij}, \tag{6}$$

where $N_x = N_y$ indicate the number of grid cells to average over in the x and y directions, respectively, and are determined by the peak wavelength L_p. The side length of the averaging area was chosen as $L_p/8$ in order to fit the square within the stereo video footprint also for the longest wave lengths in the EKOK data set. From $\bar{\eta}(t)$, wave groups can be identified with minimal influence of short, riding wave components which may cause unnecessary splitting of the dominant wave groups. An example of a filtered mean sea surface time series is shown in Figure 4a.

4.1.1. The Run Threshold Method

By the simplest definition, a wave group is a train of high dominant waves appearing in a consecutive fashion. In a surface elevation time series, for example, such a wave train would show an uninterrupted sequence of waves higher than some prescribed threshold. Following Kimura (1980), we use a threshold wave height of H_{rms}, the root-mean-square wave height, where individual wave heights are estimated from the 20-min $\bar{\eta}(t)$ records in the EKOK data set using the zero-upcrossing method (Holthuijsen, 2007). Each run of waves exceeding H_{rms} and longer than one peak wave period in duration is defined as a wave group.

4.1.2. The Hilbert Spectrum

Another common approach to detecting wave groups is by examining the instantaneous energy of the wave signal. This can be performed by analyzing the envelope of the wave signal by, for example, the Hilbert transform (Bitner-Gregersen & Gran, 1983), the wavelet transform (Donelan et al., 1996), or convolution-based smoothing techniques (Funke & Mansard, 1980). In this study, we apply the empirical mode decomposition (EMD) based method introduced by Veltcheva and Guedes Soares (2007), in which the instantaneous wave energy IE is estimated from the Hilbert spectrum (defined below) of the mean sea surface elevation time series. Wave groups are defined by the crossings of the IE signal above and below its record-mean level, as in Veltcheva and Guedes Soares (2016). Moreover, as for the H_{rms} threshold method, we require the wave groups identified by the IE threshold to be at least one peak wave period in length.

EMD is a method developed by Huang et al. (1998) for extracting the local frequency content of a broadband, multi-component (and potentially nonlinear and non-stationary) signal. The principle behind EMD analysis consists of decomposing a time series into a finite number of single-component basis functions called intrinsic mode functions (IMF) and a residual trend, the superposition of which reconstructs the original signal. The IMFs are determined via an iterative sifting process in which each IMF by definition is an oscillating signal containing an almost equal number of local extrema and zero-crossings (the respective numbers can differ at most by one), and has a zero mean at all points between the envelopes connecting the local IMF minima and maxima. Defined in this way, each IMF represents one mode of oscillation of the original signal, and the distances between consecutive IMF extrema represent the signal's intrinsic time scales. The residual component typically lacks a full oscillation and thus can be viewed as describing a background trend. In contrast to conventional Fourier decomposition, in which the signal is decomposed into simple trigonometric basis functions, the IMFs can be both amplitude and frequency modulated. As a result, the EMD method is not limited by the strict requirement of signal stationarity that applies to Fourier analysis, and can also be applied successfully to nonlinear signals (Huang et al., 1998).

The EMD method allows us to represent the variation of the wave signal's energy content in both time and frequency. An analytic function $Z_j(t)$ can be estimated for each IMF by

$$Z_j(t) = X_j(t) + iY_j(t), \tag{7}$$

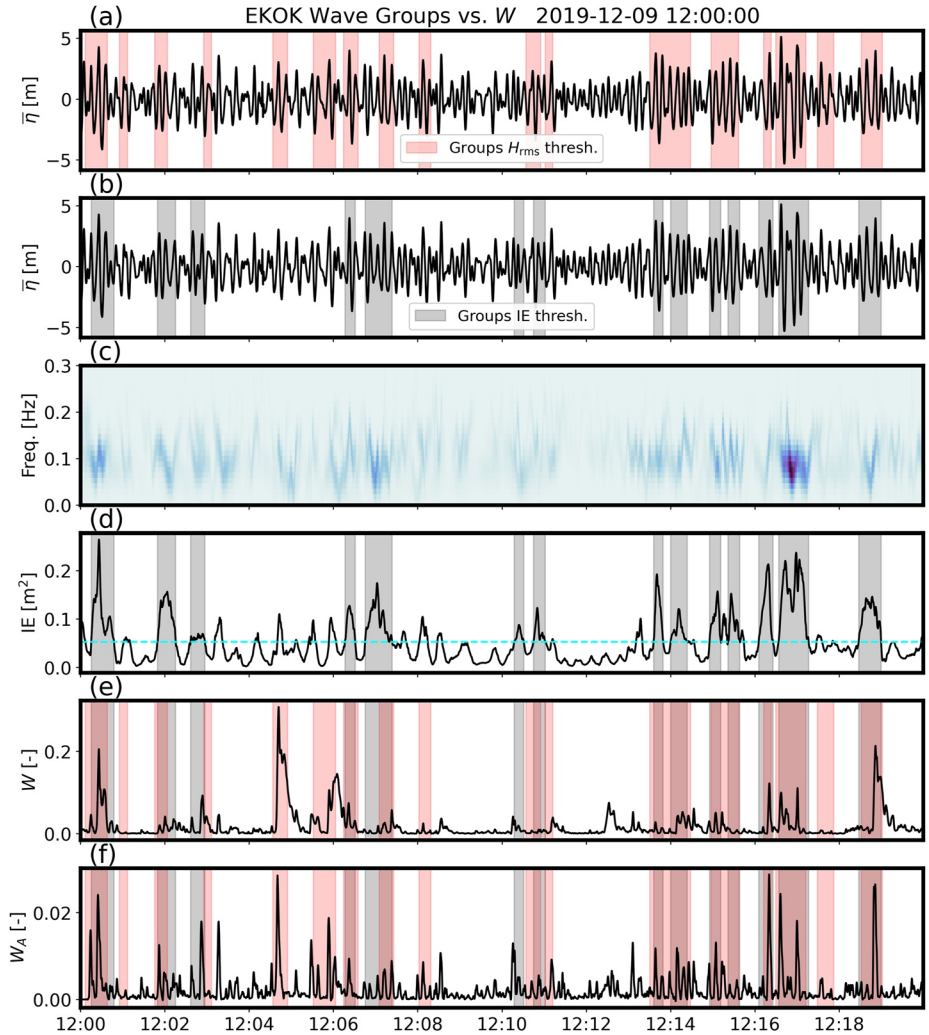

Figure 4. Sample coherent time series from the EKOK data set. (a) and (b) The stereo video spatially averaged sea-surface elevation $\bar{\eta}$. (c) The Hilbert spectrum of $\bar{\eta}$. (d) The instantaneous wave energy IE. (e) The instantaneous total whitecap coverage W. (f) The instantaneous active whitecap coverage W_A. In (a), wave groups defined by the H_{rms} threshold are shaded red, and in (b) wave groups defined by the IE threshold are shaded gray. The record-mean level of IE, that is, the wave group threshold, is marked with a horizontal dashed line in (c). Both the IE and H_{rms} group definitions are plotted in (e) and (f).

where the conjugate pair $X_j(t)$ and $Y_j(t)$ are the j-th IMF and its Hilbert transform, respectively, and i is the imaginary unit. The analytic function (7) can be used to estimate the envelope amplitude and a well-defined instantaneous frequency for each IMF. For the purposes of the current study, the instantaneous amplitude and frequency are used to quantify the group modulation—in both amplitude and frequency—of the wave signals $\bar{\eta}(t)$ in terms of the Hilbert spectrum $\mathcal{H}(f,t)$. The Hilbert spectrum was defined by Huang et al. (1998) as the distribution of the squared amplitude envelopes of all IMFs in both time and frequency. Following Veltcheva and Guedes Soares (2016; their Equation 19), integrating the Hilbert spectrum over all frequencies gives the instantaneous energy IE(t) of the wave signal,

$$\mathrm{IE}(t) = \int_{f_1}^{f_2} \mathcal{H}(f,t)\,\mathrm{d}f. \tag{8}$$

Sample time series of $\mathcal{H}(f,t)$ and the associated instantaneous wave energy IE(t) are shown in Figures 4c and 4d.

Advantages of the Hilbert spectral approach—also known as the Hilbert-Huang Transform (HHT)—over more traditional Fourier and wavelet-based time-frequency energy distributions applied to nonlinear phenomena, such

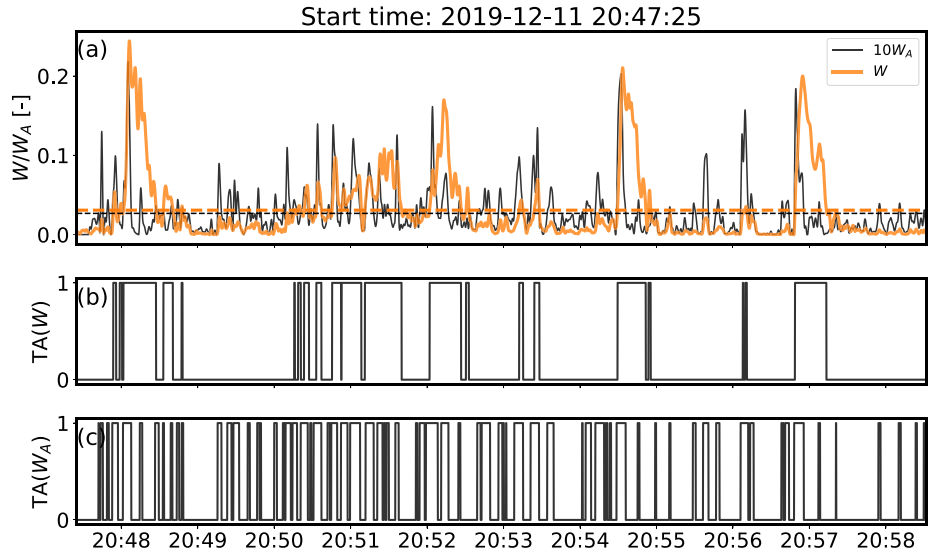

Figure 5. (a) Sample time series from the PAPA data set of the instantaneous total whitecap coverage W and the active whitecap coverage W_A, scaled by a factor of 10 to be visible on the same figure as W. See Figures 3d–3f for snapshots from the same record. The time mean levels of $\overline{W}$ and $10\overline{W_A}$ are marked with dashed lines. (b) The binary telegraph approximation (TA) time series of W, in which only mean-level zero-crossing information is retained while amplitude variations are ignored. (c) The TA time series of W_A.

as oceanic surface waves, include higher frequency resolution (due to the local nature of the intrinsic time scales represented by the IMFs) and its resilience against the impact of spurious harmonic wave components inherent in the Fourier spectral representation of nonlinear signals (Huang et al., 1999).

4.2. Intermittency Analysis

We investigate the intermittency of wave breaking in both the EKOK and PAPA data sets by analyzing the time variability of the whitecap coverage data. For this we employ the telegraphic approximation (TA) formalism on the instantaneous time series of W and W_A. The TA form of a time series is a binary sequence in which only the zero-crossing information is retained, while amplitude variations are disregarded (Sreenivasan & Bershadskii, 2006). The TA of a zero-mean time series $s(t)$ is defined as

$$\mathrm{TA}(s) = \frac{1}{2}\left(\frac{s(t)}{|s(t)|} + 1\right). \tag{9}$$

The TA time series assumes a value of one when the zero-level threshold is exceeded and zero otherwise. Examples of the TA of a record of coherent W and W_A time series from the PAPA data set are shown in Figure 5. Because the fractional whitecap coverage is a positive semi-definite quantity, we subtract the record mean before computing the TA time series of W and W_A.

It has been shown for various intermittent stochastic processes that the spectral density of the TA of a time series is related to the spectral density of the original series in regions where the original spectrum displays power-law behavior. Specifically, if the original spectrum decays as f^{-n}, then the spectrum of the TA series is expected to decay as f^{-m}, where

$$m = \frac{n+1}{2}. \tag{10}$$

For $n > 1$, $m < n$, which has been interpreted as an indication of the TA spectrum's higher memory content due to the decorrelating effect of amplitude variations on the original spectrum (Sreenivasan & Bershadskii, 2006).

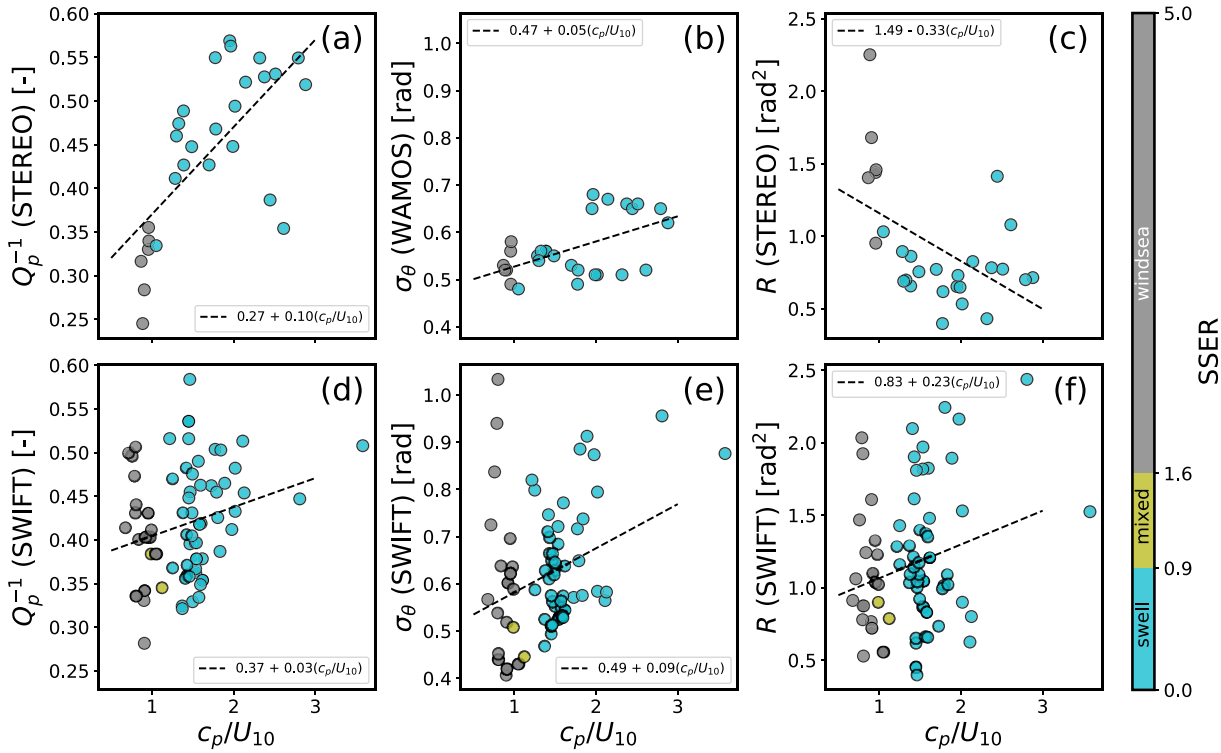

Figure 6. Various spectral width parameters from the two data sets as a function of the wave age c_p/U_{10}: (a) the spectral bandwidth in frequency estimated by Q_p^{-1}. (b) The directional spread σ_θ. (c) The multidirectionality coefficient $R = \sigma_\theta^2 Q_p^2/2$. The upper row relates to the EKOK data set, and the lower row relates to the PAPA data set. The dashed lines are the linear least-squares fits to the scatter plots. The scatter points are colored based on the sea-swell energy ratio of the wave energy spectra.

5. Results and Discussion

5.1. Wave Field Groupiness in the Field Data Sets

Figures 6 and 7 sum up the degree of groupiness of the wave fields encountered during the EKOK and PAPA video acquisition periods analyzed in this study. The comparisons of spectral width parameters against wave age c_p/U_{10} in Figures 6a and 6d, support the widely assumed relationship between spectral narrowness (i.e., low Q_p^{-1}) and young sea states, although the relationship appears more robust in the EKOK data set, collected in the North Sea, than in the North Pacific PAPA data set. This may reflect the bias of the JONSWAP parameterization toward fetch-limited sea states typical for the North Sea; however, the number of data points in the EKOK data set is too limited to draw confident conclusions on this matter. The directional spread σ_θ exhibits a similar, growing trend with aging seas in both data sets, but the multi-directionality parameter R displays inconsistent behavior between the data sets, owing mainly to the large range of directional spreads estimated from the SWIFT wave buoy motions in the PAPA data set.

Figure 7 compares the distributions of mean group duration T_g, normalized by the peak wave periods T_p, calculated with the IE and H_{rms} threshold methods in the two data sets (see Sections 4.1.1 and 4.1.2). The EKOK group durations are calculated from the stereo video mean sea surface elevation time series $\bar{\eta}$, and the PAPA group durations are computed from SWIFT buoy heave time series. Heave records from SWIFTs were not available at all video acquisition periods, however, and the lengths of individual heave time series ranged between 6 and 8 min. The EKOK wave groups display behavior consistent with the JONSWAP model, with prominent, long wave groups being somewhat more prevalent during sea states with narrow wave spectra in both frequency and directional spread. The PAPA group durations, on the other hand, display less consistency with the behavior expected and observed in the North Sea.

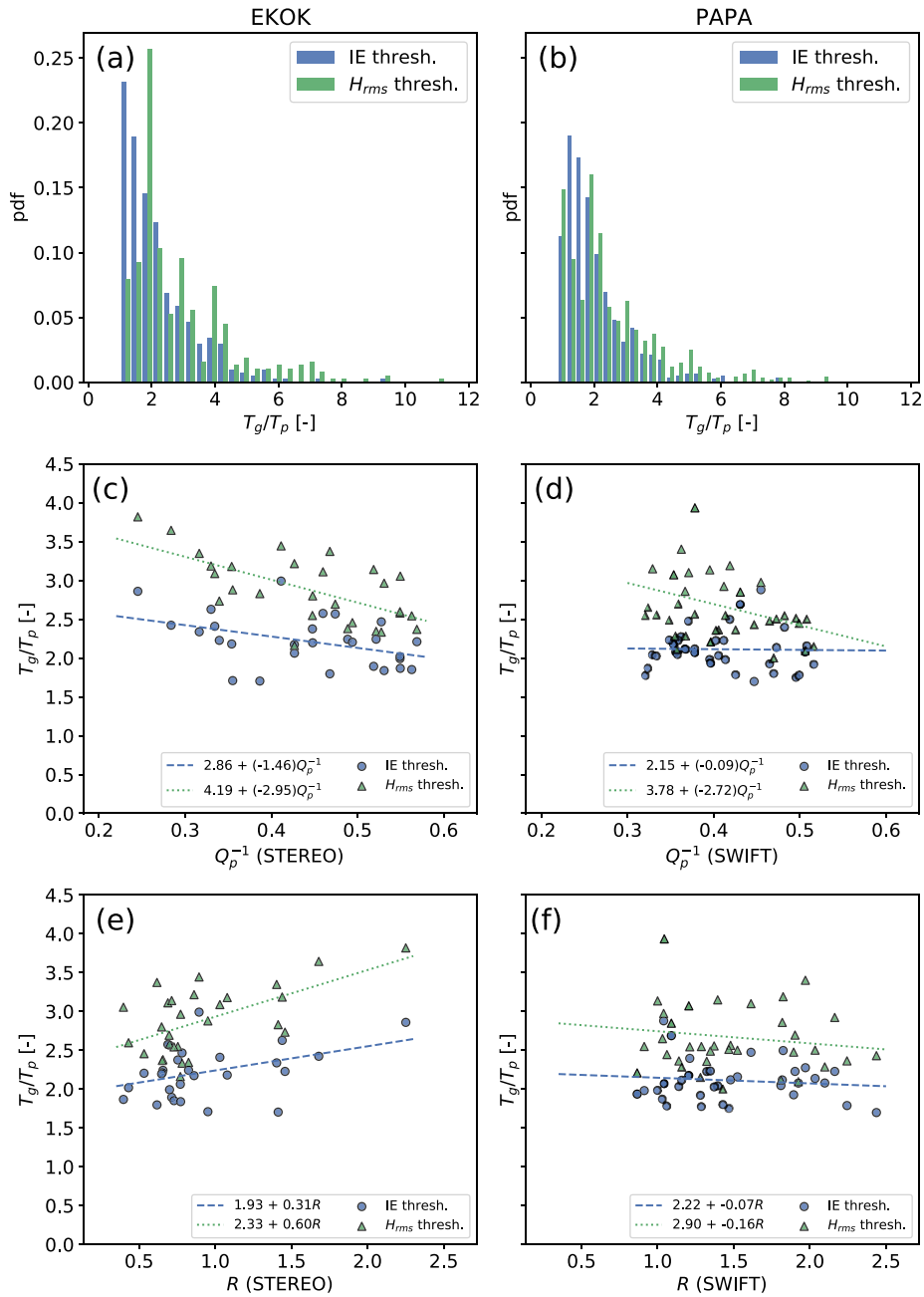

Figure 7. Left column: comparison of group durations in the EKOK data set defined by the Hilbert spectrum-based IE criterion of Veltcheva and Guedes Soares (2016) and the run-based H_{rms} criterion of Kimura (1980). (a) Histograms of the distributions of group durations T_g normalized by the peak periods T_p of the stereo video scalar spectra. (c) Normalized group durations as a function of the spectral bandwidth parameter Q_p^{-1}. (e) Normalized group durations as a function of the multidirectionality coefficient $R = \sigma_\theta^2 Q_p^2/2$, where the directional spread σ_θ is obtained from the WAMOS product, while Q_{p} is the peakedness of the stereo spectra. The dotted and dashed lines in (b) and (c) are the least-squares linear fits to the $T_{\mathrm{g}}/T_{\mathrm{p}}$ scatter points. The right column shows the same parameters, estimated from the SWIFT buoy data in the PAPA data set.

5.2. Wave Group-Enhanced Breaking

5.2.1. Instantaneous W and W_{A} Distributions

Figure 8 shows the probability distributions of the instantaneous values of W and W_{A} spanning the full EKOK data set that coincide with wave groups detected in the time series of $\bar{\eta}$, versus W and W_{A} coinciding with the segments of $\bar{\eta}$ that fall between the wave groups, as illustrated in the example in Figure 4. The time series of instantaneous

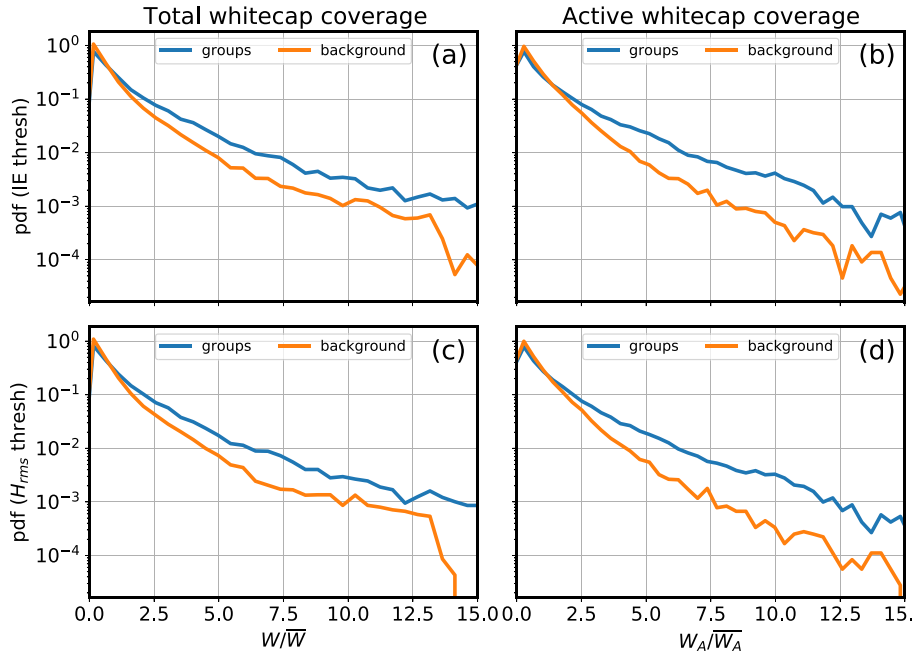

Figure 8. (a) and (c) Probability distributions of the relative instantaneous whitecap coverage $W/\overline{W}$ within the EKOK stereo camera footprint during wave group passage (blue curves) and between wave groups (orange curves). In (a) the wave groups are defined with the instantaneous wave energy (IE) threshold method, and in (c) the groups are defined as runs of high waves exceeding H_{rms} in height. (b) and (d) As in (a) and (c), but for the relative active whitecap coverage $W_A/\overline{W_A}$. The probability distributions are composed from all twenty-eight 20-min records in the EKOK data set, and truncated at relative whitecap coverage values of 15 to exclude the poorly sampled and noisy distribution tails.

W and W_{A} have been low-pass filtered with a 0.5-Hz cutoff in order to minimize the effects of high-frequency noise due to, for example, short-lived sun glints. To verify that the group-background distributions are insensitive to the choice of wave group definition, we show the results for both the run threshold-based group definition of Kimura (1980) and the IE-based group definition of Veltcheva and Guedes Soares (2007). Irrespective of the group definition employed, Figures 8a and 8c show that wave groups are associated with an approximately two to threefold enhancement of the probability of encountering elevated values of total whitecap coverage W relative to its record-wise mean value, $\overline{W}$. As shown in Figures 8b and 8d, this group-related enhancement in probability grows to approximately fivefold for high values of the relative active whitecap coverage $W_A/\overline{W_A}$.

The disparity between the W and W_{A} group-background distributions is likely to be influenced by our choice of method for W_{A} classification. We follow the approach of Schwendeman and Thomson (2015b), which isolates only the leading edges of propagating whitecaps. We argue that our estimates of W_{A} therefore provide a better indication of the initiation of breaking and maximum breaking extent (in terms of breaking crest length) than our estimates of W. The latter includes the influence of decaying foam patches that likely do not contribute to active breaking, but which, especially in instances of large-scale breaking events, may linger for several wave periods. As has been pointed out before (Mironov & Dulov, 2008), the total area of large whitecaps, the main contributor to the instantaneous value of W, may continue to grow for a period of time beyond the instant of maximum active breaking due to the dispersion and advection of the foam patch due to the orbital motion of the waves. For these reasons, elevated values of W may persist for several wave periods after the group that initiated the breaking has passed, whereas spikes in W_{A} effectively pinpoint the dominant wave-group phase at which the breaking is in its most active stage.

The consistently elevated probability of encountering high-amplitude values of W (indicative of large scale breaking events) during wave groups compared to between groups suggests that the prevalence of dominant wave breaking is related to the groupiness of the wave field, as reported in the early investigations of Donelan et al. (1972) and Holthuijsen and Herbers (1986). However, due to the variable decay rate of whitecaps, dependent on, for example, breaking strength (Callaghan et al., 2012), enhanced values of W may persist within the camera footprint for a longer period than the passage of wave groups, making it difficult to verify the true group-phase

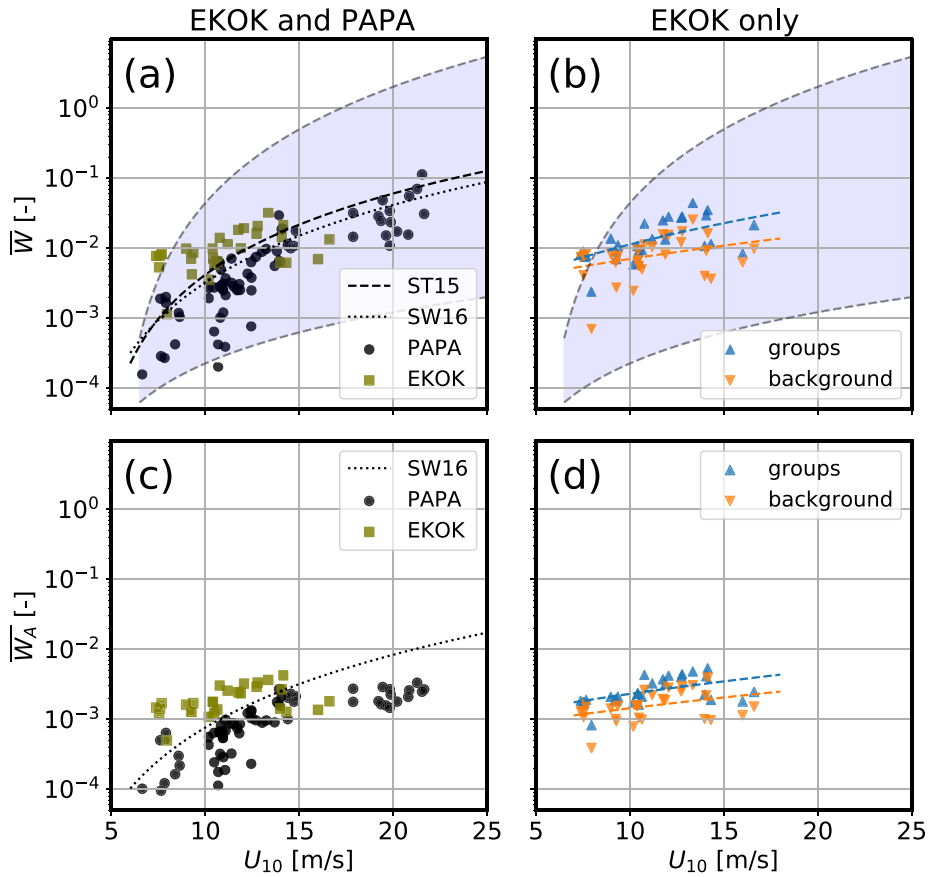

Figure 9. (a) Time-averaged total whitecap coverage $\overline{W}$ as a function of wind speed U_{10}, estimated from the PAPA image sequences (circles) and EKOK image sequences (squares). The dashed and dotted curves show the functional fits of ST15 (Schwendeman & Thomson, 2015b) and SW16 (Scanlon & Ward, 2016), respectively. The shading covers the reported 90% confidence interval around the ST15 fit. (b) The mean EKOK W values averaged during wave group passage (upward-pointing triangles) and between wave groups (downward-pointing triangles). The ST15 confidence interval is also included in shading. (c) The time-averaged active whitecap coverage $\overline{W}_A$ as a function of wind speed, with the Scanlon and Ward (2016) fit shown with the dotted curve. (d) As (b), but for the EKOK active whitecap coverage. The dashed lines in (b) and (d) are cubic fits of the form Equation 12 to the group/background data points. The wave group definition applied in (b) and (d) is the IE threshold method.

origin of all high W values in Figures 8a and 8c. However, the stronger group-related enhancement visible in the group versus background distributions of W_A (Figures 8b and 8d) suggest that the group modulation of breaking is a significant mechanism in determining breaking location in time and space. However, as seen in Figure 5, the amplitude of W_A may be a weaker indication of the full scale of breaking than the amplitude of W. This result likely follows from the W_A thresholding procedure which primarily isolates thin slices of the rapidly propagating, actively breaking crests (see Figure 3).

5.2.2. Time-Averaged W and W_A

Time-averaged values of W and W_A, denoted $\overline{W}$ and $\overline{W_A}$, are plotted in Figure 9 against the neutral 10-m wind speed U_{10}. The averaging periods for EKOK estimates of W and W_A are 20 min, while the variable-length PAPA estimates were averaged over periods ranging from 10 to 20 min. The PAPA wind speeds shown are 10-min averages. The mean total whitecap coverage $\overline{W}$ data points from both the EKOK and PAPA data sets, plotted in Figure 9a, are compared to empirical fits from two fairly recent studies, namely Schwendeman and Thomson (2015b; ST15) and Scanlon and Ward (2016; SW16). The ST15 fit was published with 90% confidence intervals, which are included in shading in Figure 9a. The ST15 data set was collected in the same geographic location as the PAPA data set using the same equipment and compiled with essentially the same processing methods. The ST15 fit was achieved with a generalized power-law function

$$\overline{W} = a(U_{10} - b)^n, \tag{11}$$

where $a = 2.81 \times 10^{-5}$, $b = 3.87$ m s^{-1}, and $n = 2.76$. Figure 9a shows a tendency of the PAPA data points to be biased somewhat below the ST15 fit. This may be related to our approach to the choice of pixel intensity threshold, which was intentionally conservative (meaning we generally applied high threshold values) in order to avoid false whitecap detection due to sun glints. The SW16 data set was collected in the North Atlantic and the Southern Ocean, and the fit of the data points of $\overline{W}$ against U_{10} was approximated with a cubic function of the form

$$\overline{W} = a(U_{10} - b)^3, \tag{12}$$

with $a = 7.84 \times 10^{-6}$ s^3 m^{-3} and $b = 2.56$ m s^{-1}. Because the SW16 fit generally lies below the ST15 fit, $\overline{W}$ data points in the PAPA data set generally correspond more closely to the SW16 fit (see Figure 9a). This is most apparent at high wind speeds ($U_{10} > 17$ m s^{-1}). The EKOK $\overline{W}$ data points, on the other hand, are in general biased higher than PAPA, especially for low wind speeds. While pixel-intensity threshold selection may influence the differences in magnitude of $\overline{W}$ between the data sets to some degree, it is reasonable to expect that the wind speed conversion from 102.3 to 10 m at EKOK is associated with markedly larger uncertainty than the 16-to-10 m conversion in the PAPA data set. Therefore, it is plausible that the U_{10} estimates are biased low rather than the $\overline{W}$ estimates being biased high at EKOK.

We remind the reader that the wind speeds U_{10} reported in this study are equivalent wind speeds for a neutrally stratified atmospheric boundary layer. While neutral winds are commonly used in whitecap coverage parameterizations (Brumer et al., 2017; Scanlon & Ward, 2016), it is known that stability effects may account for appreciable deviations of the true wind from the neutral estimate, especially at short timescales (Kara et al., 2008). Whilst a number of studies have investigated the effect of explicitly accounting for stability in $W(U_{10})$ parameterizations, the results have largely proved inconclusive on the significance of its impact (Monahan & Woolf, 1989; Paget et al., 2015). The whitecap data analyzed in this study were mainly collected in wind-forced conditions in the open ocean, with air-sea temperature differences associated with unstable or neutral atmospheric stratification (not shown). We therefore anticipate stability-related effects on our U_{10} estimates to be rather small, at least in comparison to the spread in the W estimates.

A physical factor worthy of consideration for the observed bias between the data sets is the difference in effective water depth between the geographical locations. Whereas the PAPA data set was collected in very deep water, the 70-m mean water depth at Ekofisk means that the dominant wave field is regularly in an intermediate water regime (Christensen et al., 2017). The topic of whether the depth-induced steepening of the dominant waves leads to more frequent wave breaking in the North Sea compared to the North Pacific is, however, outside the scope of the current study, and will be addressed in future work. Furthermore, despite the apparent bias between the $\bar{W}$ estimates in the two data sets, individual data points from both mostly remain confined within the 90% confidence intervals reported for the ST15 data set.

The time-averaged $\overline{W_A}$ estimates (Figure 9c) are compared to the SW16 fit, in which actively breaking whitecaps were separated manually from decaying remnant foam patches. The SW16 fit for W_A follows Equation 12 with $a = 1.39 \times 10^{-6}$ s^3 m^{-3} and $b = 1.80$ m s^{-1}. While our $\overline{W_A}$ estimates reasonably follow the ST16 fit for low-to-intermediate wind speeds, the higher-windspeed (> 15 m s^{-1}) $\overline{W_A}$ data points appear to flatten out and remain markedly below the ST16 curve. This behavior likely reflects our selected method for W_A detection (Schwendeman & Thomson, 2015b), which isolates fairly narrow regions of propagating whitecapping crests for very short durations (i.e., single frames). ST16, on the other hand, used the manual active breaker detection methodology described by Scanlon and Ward (2013), in which individual whitecaps are classified as either actively breaking or remnant foam based on the wave crest locations, the visual intensity and image texture. It was later found (Scanlon et al., 2016) that the active whitecap estimates thus calculated were a better match to the dissipation from breaking waves estimated by a wave model than the total whitecap coverage. Moreover, while the pixel "flipping" method for W_A detection was described by ST15, they did not report estimates of $\overline{W_A}$ made using the technique. The authors used the technique in a later study (Schwendeman & Thomson, 2017) to isolate breaking crests, but again no $\bar{W}_A$ estimates were reported. To our knowledge, Figure 9c is the first reported result in which the ST15 technique has been applied for producing estimates of $\overline{W_A}$.

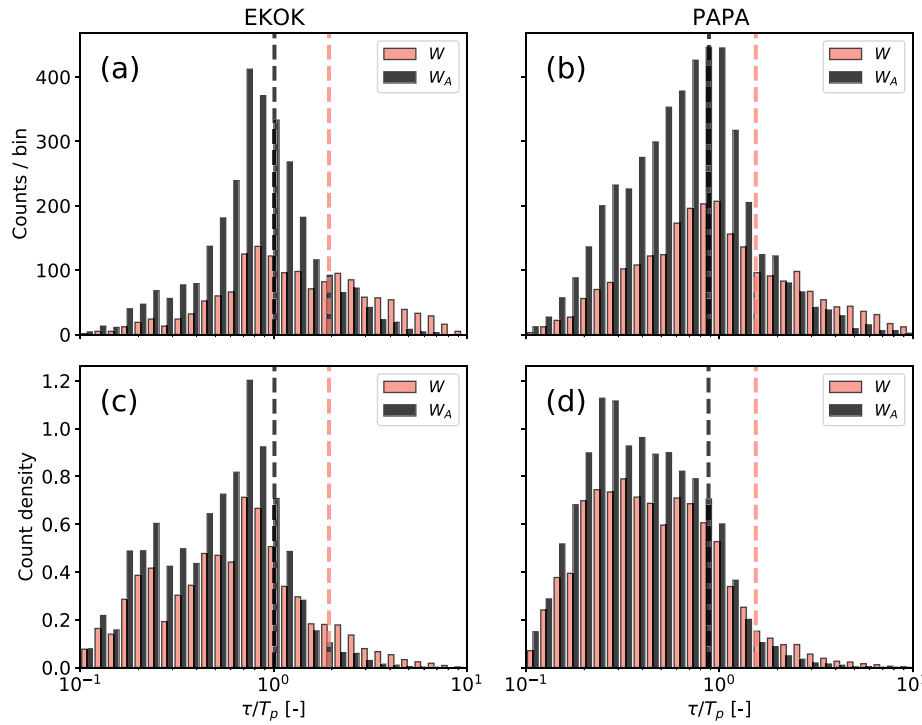

Figure 10. Histograms of the time periods τ between successive mean-level up-crossings of the time series of W and W_A, normalized by the prevailing peak wave periods T_p. The histograms are estimated with 30 logarithmically spaced bins between 0.1 and 10. Histograms relating to W are colored red and those relating to W_A are colored black. The mean τ/T_p values for W and W_A are marked with dashed red and black vertical lines, respectively. Results from the EKOK data set are shown in the left column, and PAPA results in the right column. The upper row (panels (a) and (b)) shows the number of values within each bin, and in the lower row (panels (c) and (d)), the counts per bin have been normalized by the product of the total number of counts and the variable bin width.

The right column of Figure 9 shows EKOK estimates of $\overline{W}$ and $\overline{W_A}$, in which the time averaging has been performed in versus between wave groups using the coherent time series of $\bar{\eta}$ from the stereo video reconstructions. As would be expected from the analysis of the instantaneous W and W_A estimates presented in Figure 8, the time-averaged values display clear wave group-induced enhancement. The apparent separation in magnitude of $\overline{W}$ and $\overline{W_A}$ when averaged during wave-group passage versus during quiescent periods suggests that the degree of wave field groupiness may be a source of the large scatter exhibited by previously reported whitecap coverage estimates (Anguelova & Webster, 2006; Brumer et al., 2017; Salisbury et al., 2013). Previous attempts at introducing wave field-dependent variables to W parameterizations have found only weak dependence of the variability of W and W_A with general wave field parameters (Albert et al., 2016; Brumer et al., 2017; Scanlon & Ward, 2016; Schwendeman & Thomson, 2015b). Our results presented in Figures 9b and 9d, however, demonstrate that wave field groupiness characteristics directly impact estimates of the whitecap coverage. Future studies may test the wave group effects on larger data sets by revisiting satellite measurements of W and controlling for wave field groupiness in terms of, for example, spectral bandwidth, peakedness, and directional spread using a spectral wave model.

5.3. Time Scales and Intermittency of the Whitecap Coverage

5.3.1. Inter-Breaking Periods

The time variability of wave breaking is investigated by analyzing the mean-level crossings of the low-pass filtered instantaneous time series of W and W_A. Since coherent sea-surface elevation records are not required for this analysis, this section includes results from both the EKOK and PAPA data sets. In Figure 10, we estimate the distributions of the time periods between consecutive mean-level up-crossings τ of the whitecap coverage records, normalized with the prevailing peak wave periods T_p, with logarithmically spaced histogram bins. The

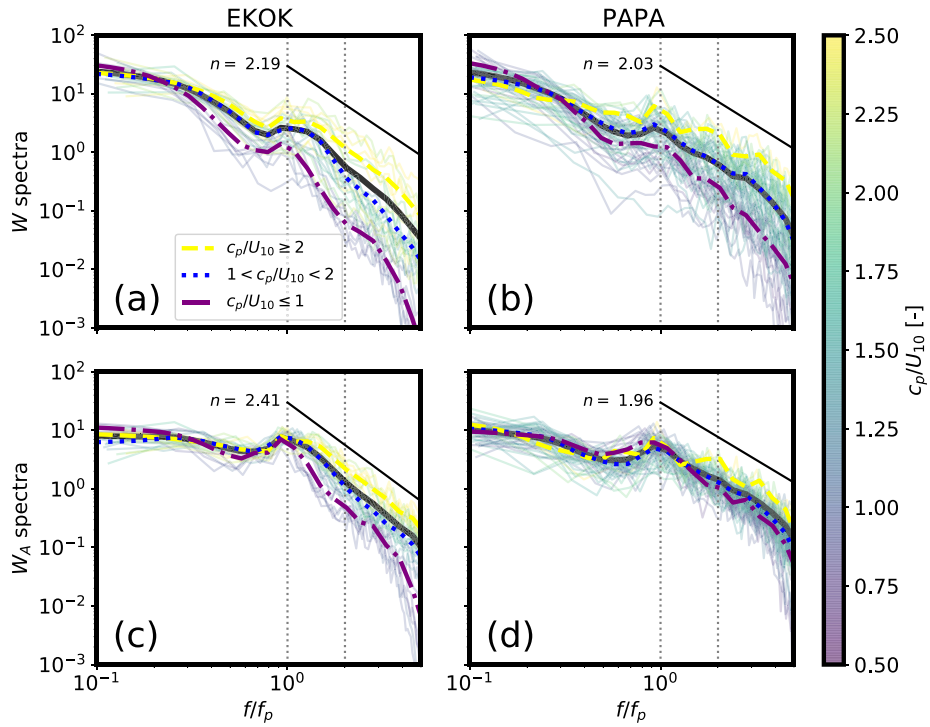

Figure 11. (a) and (b) Spectral densities of the instantaneous total whitecap coverage W. (c) and (d) Spectral densities of the instantaneous active whitecap coverage W_A. The spectra from the EKOK data set are in the left column, and the PAPA spectra are in the right column. The x axes are the spectral frequencies normalized by the peak wave frequencies f_p during each W and W_A acquisition period. The locations of $f/f_p = 1$ and $f/f_p = 2$ are marked with dotted vertical lines. The color scaling of the individual spectra (thin curves) indicates the prevailing wave age c_p/U_{10}. The thick solid curves (black) are the means of all individual spectra. The dashed yellow curves are the mean spectra for wave ages above 2, the dotted blue curves are the mean spectra for wave ages between 1 and 2, and the dash-dotted purple curves are the mean spectra for wave ages below 1. The steep decay of the young-sea spectra at high relative frequencies may be partly due to the low-pass filtering of the W and W_A time series at 0.5 Hz. The power-law fits to the full mean spectra above $f/f_p = 1$ are plotted with solid lines, with the power-law exponents n indicated next to the fit lines.

distributions displayed by counts per bin (Figures 10a and 10b) exhibit skewed unimodal or weakly bi-modal shapes, with mode values approximately at $\tau/T_p = 1$ or somewhat lower. In comparison, the mean τ/T_p values of all total whitecap coverage time series W are $\tau/T_p = 1.93$ and $\tau/T_p = 1.54$ for the EKOK and PAPA data sets, respectively. The equivalent mean values of all W_A time series are $\tau/T_p = 1.01$ and $\tau/T_p = 0.88$ for EKOK and PAPA, respectively. When the bin-wise counts are normalized by the products of the total number of counts and the variable bin widths (Figures 10c and 10d), the distributions assume more bi-modal shapes, with modes skewed at even lower values of τ/T_p.

The tendency of the instantaneous W_A records to exhibit mean-upcrossings at a frequency very near the peak wave frequency supports results from previous studies showing preferential breaking of shorter wave components at the crests of dominant waves (Dulov et al., 2002; Yurovsky et al., 2017). The nearly twofold difference in the mean values of τ/T_p between W and W_A in both data sets suggests that the mean-upcrossings of W_A capture a larger portion of small-scale breaking occurring during or between large-scale or high-impact breaking events than the mean-upcrossings of W, in which clusters of elevated values may persist for several wave periods as a result of slowly dissipating foam patches which may mask smaller-scale intermediate breaking events (see the example time series in Figure 5). Moreover, the mean-upcrossings of W display similar periodicity to the observations of Donelan et al. (1972), who observed dominant waves breaking at a frequency related to approximately twice the peak wave period.

5.3.2. Spectral Density of W and W_A

A spectral representation of the whitecap coverage is shown in Figure 11, where frequency spectra are estimated from each individual time series of instantaneous W and W_A in both the EKOK and PAPA data sets, and colored

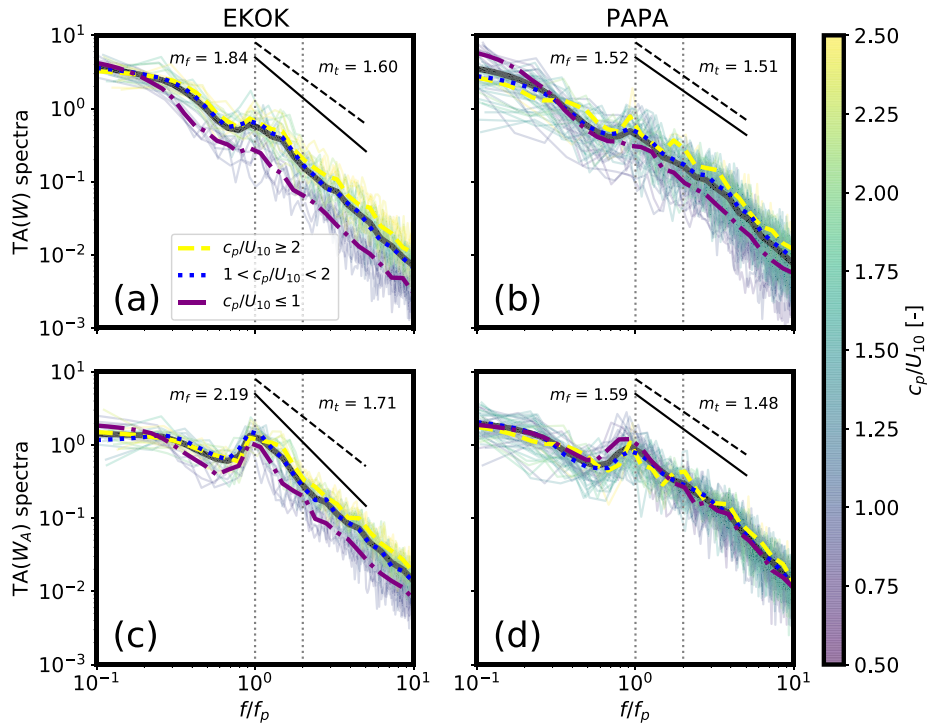

Figure 12. As Figure 11, but for spectra of the TA of the total whitecap coverage W (upper row), and spectra of the TA of the active whitecap coverage W_A (lower row). Color scaling as in Figure 11. The solid lines are the power-law fits to the mean TA spectra (solid black curves) in the tail region between $f/f_p = 1$ and 2 (same interval as in Figure 11), with slopes indicated by m_f. The dashed lines are the theoretical power-law slopes based on the spectral slopes n in Figure 11 as predicted by Equation 10, with theoretical slope coefficients indicated by m_t.

according to the wave age of the underlying sea state. As shown in Figure 11a and 11b, the individual W spectra in both data sets exhibit considerable scatter. A few distinguishing features can, however, be identified from the mean spectra classified by wave age intervals. The high energy content at the lowest frequencies visible in all mean W spectra is most likely due to the slow decay of large foam patches from large scale breaking events. At all wave ages a secondary peak, or at least a flattening of the spectral slope, is visible close to the peak wave frequency. The secondary peak is followed by decaying spectral density with a tendency toward power-law behavior, although the spectral tail slopes display some variation across wave ages and data sets. At the highest relative frequencies, the slopes of the young sea spectra may be somewhat affected by the low-pass filtering of the W and W_A time series at 0.5 Hz. The high wave age ($c_p/U_{10} \geq 2$) mean W spectrum in the PAPA data set also appears to have a third peak at approximately $f/f_p = 2$; however, the significance of this third peak is questionable, as the high wave age mean spectrum of the PAPA data set is averaged over only four separate spectra. The estimated power-law fits to the $f/f_p > 1$ regions of the total mean spectra are also included in Figures 11a and 11b, with power-law exponents $n = 2.19$ and 2.03 for the EKOK and PAPA mean W spectra, respectively.

The W_A spectra (Figures 11c and 11d) display a more pronounced peak at $f/f_p = 1$, reflecting the more localized nature of the W_A estimate, in which breaking events are characterized by short-lived spikes focused at the points in time when the breaking crests attain their maximum extent. Compared to the W spectra, the W_A spectra also display somewhat less scatter at high frequencies. The power-law exponents of the mean W_A spectra are estimated as $n = 2.41$ and $n = 1.96$ for EKOK and PAPA, respectively.

5.3.3. Intermittency Spectra

A complementary representation to the whitecap coverage spectra in Figure 11 is shown in Figure 12 with the spectral densities of the TA of the W and W_A time series. Since the TA representation only retains information of the time separation between successive crossings of the mean W and W_A levels, such that the de-correlating effects of amplitude variations are minimized, previously published results on general stochastic processes (Cava et al., 2012; Sreenivasan & Bershadskii, 2006) give reason to expect that the TA spectra exhibit more consistency

than the W and W_A spectra shown in Figure 11. Indeed, this behavior is evident, especially in the tail regions of all TA spectra, where the spectral slopes display less variation with wave age, and the power-law behavior extends to higher relative frequencies than in the W and W_A spectra. The spectral peak at the peak wave frequency is also pronounced, especially in the TA spectra of W_A, shown in Figures 12c and 12d. The fitted power-law exponents m_f of all mean TA spectra show reasonable agreement with the theoretical slopes m_t, predicted by the relationship in Equation 10, suggesting that the intermittency characteristics of W and W_A are of a similar nature to other stochastic processes occurring in both natural and controlled environments.

5.3.4. Comparison to Prior Observations

The analyses of the time scales of breaking presented in this section point toward a universal breaking at a period that is closely linked to the period of the dominant waves. This supports the amplitude analysis presented in Section 5.2, which showed enhanced breaking activity linked to the passage of energetic wave groups. Dominant wave crests have also been shown to be the preferential breaking regions for waves of various scales in previous field studies (Donelan et al., 1972; Dulov et al., 2002, 2021; Holthuijsen & Herbers, 1986; Yurovsky et al., 2017). A marked contrast exists, however, between the magnitude of long wave modulation of wave breaking in our results, which show a 2–5 fold enhancement of breaking probability attributed to wave groups, compared to those of Dulov et al. (2002, 2021) who found modulation factors as high as 20–24. It is, however, important to keep in mind that our analysis sorts long waves into two categories, namely wave groups and the "background" wave field. Both of these categories consist of dominant waves, a portion of which are related to wave breaking of varying scales as shown in Figure 4. The analyses of Dulov et al. (2002, 2021), on the other hand, examine the modulation of breaking by long waves irrespective of their amplitude and group structure. With this in mind, our results should be viewed as complementary, not contradictory, to those of Dulov et al. (2002, 2021).

It is important to note that our analysis presented herein is relatively ambiguous regarding the scale (e.g., spatial extent or breaking strength) of the breaking that occurs at dominant wave-related periodicity. Previous studies on the distributions of crest-lengths per unit area and crest propagation speed have found that dominant-wave breaking accounts for only a fraction of the total breaking rate in typical wind-forced sea states, with the majority of breaking occurring at much shorter wave scales with mean breaking crests speeds typically of the order of half the phase speeds of peak waves or less (Kleiss & Melville, 2010; Romero, 2019; Schwendeman et al., 2014; Thomson et al., 2009). Our results should not be considered contradictory to these previous findings, but should be viewed as further evidence that dominant-wave modulation is an important mechanism in driving wave breaking at a wide range of scales.

6. Conclusions

We have analyzed the variability of high-temporal resolution oceanic whitecap coverage with the underlying dominant wave group structure using stereo video observations from a platform in the central North Sea. The observations show enhanced probability of occurrence of high instantaneous whitecap coverage coincident with wave group passage, which implies that wave groupiness is associated with larger scale wave breaking activity and extent (Figure 8). The group enhancement of the whitecap coverage is apparent both in the instantaneous total whitecap coverage W and the whitecap coverage related to actively breaking wave crests W_A, although the difference between intra-group and inter-group whitecap coverage is more pronounced for W_A (approximately threefold for W vs. a fivefold enhancement for W_A). This result was shown to be insensitive to the specific definition used to distinguish wave groups from the background sea state. Wave groups were also shown to lead to enhanced values of time-averaged W and W_A compared to quiescent periods. This result suggests that wave field groupiness may be a source of scatter among previously published whitecap coverage data sets.

Analyses of the time variability of the instantaneous W and W_A data showed a tendency toward periodicity at time scales near the peak wave period, supporting previous observations of preferential breaking of short wave components near the crests of long waves. The consistency of this result was substantiated by the inclusion of a second whitecap coverage field data set collected with ship-based video cameras in a wide range of environmental conditions in the North Pacific.

Data Availability Statement

Data will be posted at https://digital.lib.washington.edu/researchworks/handle/1773/48143. Whitecap thresholding and ship motion correction codes used in the analysis can be found at https://github.com/mikapm/ship-whitecaps.

Acknowledgments
Mika Petteri Malila received funding from the Valle Foundation for a scientific stay at the University of Washington in 2019–2020. The Ekofisk stereo camera system was installed with support from the funding partners ConocoPhillips Norway and Equinor ASA through the StereoWave joint industry project which we gratefully acknowledge. Additional funding was provided by the European Union's Horizon 2020 Research and 391 Innovation Programme under grant agreement 821 001. We would like to express our gratitude to Lars Bahr (ConocoPhillips Norway) for his tireless technical support. The image processing was in part carried out on the post-processing infrastructure of the Norwegian Meteorological Institute. Our thanks to Nico Budewitz and Roger Storvik for their continued support. We also wish to thank the captain and crew of R/V Sikuliaq, as well as APL-UW field engineers Joe Talbert and Alex de Klerk, for their help in collecting the North Pacific cruise data.

References

Adcock, T. A. A., Taylor, P. H., Yan, S., Ma, Q. W., & Janssen, P. A. E. M. (2011). Did the Draupner wave occur in a crossing sea? *Proceedings of the Royal Society A: Mathematical, Physical & Engineering Sciences*, *467*(2134), 3004–3021. https://doi.org/10.1098/rspa.2011.0049

Agrawal, Y. C., Terray, E. A., Donelan, M. A., Hwang, P. A., Williams, A. J., Drennan, W. M., et al. (1992). Enhanced dissipation of kinetic energy beneath surface waves. *Nature*, *359*(6392), 219–220. https://doi.org/10.1038/359219a0

Albert, M. F., Anguelova, M. D., Manders, A. M., Schaap, M., & de Leeuw, G. (2016). Parameterization of oceanic whitecap fraction based on satellite observations. *Atmospheric Chemistry and Physics*, *16*(21), 13725–13751. https://doi.org/10.5194/acp-16-13725-2016

Anguelova, M. D., & Webster, F. (2006). Whitecap coverage from satellite measurements: A first step toward modeling the variability of oceanic whitecaps. *Journal of Geophysical Research: Oceans*, *111*(C3). https://doi.org/10.1029/2005jc003158

Babanin, A. V. (2011). *Breaking and dissipation of ocean surface waves*. Cambridge University Press.

Babanin, A. V., Chalikov, D., Young, I., & Savelyev, I. (2007). Predicting the breaking onset of surface water waves. *Geophysical Research Letters*, *34*(7). https://doi.org/10.1029/2006gl029135

Babanin, A. V., Waseda, T., Kinoshita, T., & Toffoli, A. (2011). Wave breaking in directional fields. *Journal of Physical Oceanography*, *41*(1), 145–156. https://doi.org/10.1175/2010jpo4455.1

Banner, M. L., Babanin, A. V., & Young, I. R. (2000). Breaking probability for dominant waves on the sea surface. *Journal of Physical Oceanography*, *30*(12), 3145–3160. https://doi.org/10.1175/1520-0485(2000)030<3145:BPFDWO>2.0.CO;2

Banner, M. L., & Melville, W. K. (1976). On the separation of air flow over water waves. *Journal of Fluid Mechanics*, *77*(4), 825–842. https://doi.org/10.1017/s0022112076002905

Banner, M. L., & Peirson, W. L. (2007). Wave breaking onset and strength for two-dimensional deep-water wave groups. *Journal of Fluid Mechanics*, *585*, 93–115. https://doi.org/10.1017/s0022112007006568

Barthelemy, X., Banner, M. L., Peirson, W. L., Fedele, F., Allis, M., & Dias, F. (2018). On a unified breaking onset threshold for gravity waves in deep and intermediate depth water. *Journal of Fluid Mechanics*, *841*, 463–488. https://doi.org/10.1017/jfm.2018.93

Benetazzo, A. (2006). Measurements of short water waves using stereo matched image sequences. *Coastal Engineering*, *53*(12), 1013–1032. https://doi.org/10.1016/j.coastaleng.2006.06.012

Benetazzo, A., Fedele, F., Gallego, G., Shih, P.-C., & Yezzi, A. (2012). Offshore stereo measurements of gravity waves. *Coastal Engineering*, *64*, 127–138. https://doi.org/10.1016/j.coastaleng.2012.01.007

Benjamin, T. B., & Feir, J. E. (1967). The disintegration of wave trains on deep water. *Journal of Fluid Mechanics*, *27*(3), 417–430. https://doi.org/10.1017/s002211206700045x

Bergamasco, F., Torsello, A., Sclavo, M., Barbariol, F., & Benetazzo, A. (2017). Wass: An open-source pipeline for 3D stereo reconstruction of ocean waves. *Computers & Geosciences*, *107*, 28–36. https://doi.org/10.1016/j.cageo.2017.07.001

Bitner-Gregersen, E. M., & Gran, S. (1983). Local properties of sea waves derived from a wave record. *Applied Ocean Research*, *5*(4), 210–214. https://doi.org/10.1016/0141-1187(83)90035-4

Brumer, S. E., Zappa, C. J., Brooks, I. M., Tamura, H., Brown, S. M., Blomquist, B. W., et al. (2017). Whitecap coverage dependence on wind and wave statistics as observed during SO GasEx and HiWinGS. *Journal of Physical Oceanography*, *47*(9), 2211–2235. https://doi.org/10.1175/jpo-d-17-0005.1

Buckley, M. P., & Veron, F. (2016). Structure of the airflow above surface waves. *Journal of Physical Oceanography*, *46*(5), 1377–1397. https://doi.org/10.1175/jpo-d-15-0135.1

Callaghan, A. H., Deane, G. B., Stokes, M. D., & Ward, B. (2012). Observed variation in the decay time of oceanic whitecap foam. *Journal of Geophysical Research: Oceans*, *117*(C9). https://doi.org/10.1029/2012jc008147

Cava, D., Katul, G. G., Molini, A., & Elefante, C. (2012). The role of surface characteristics on intermittency and zero-crossing properties of atmospheric turbulence. *Journal of Geophysical Research: Atmospheres*, *117*(D1). https://doi.org/10.1029/2011jd016167

Chella, M. A., Tørum, A., & Myrhaug, D. (2012). An overview of wave impact forces on offshore wind turbine substructures. *Energy Procedia*, *20*, 217–226. https://doi.org/10.1016/j.egypro.2012.03.022

Christensen, K. H., Carrasco, A., Bidlot, J.-R., & Breivik, Ø. (2017). The "shallow-waterness" of the wave climate in European coastal regions. *Ocean Science*, *13*(4), 589–597. https://doi.org/10.5194/os-13-589-2017

Derakhti, M., & Kirby, J. T. (2016). Breaking-onset, energy and momentum flux in unsteady focused wave packets. *Journal of Fluid Mechanics*, *790*, 553–581. https://doi.org/10.1017/jfm.2016.17

Derakhti, M., Kirby, J. T., Banner, M. L., Grilli, S. T., & Thomson, J. (2020). A unified breaking onset criterion for surface gravity water waves in arbitrary depth. *Journal of Geophysical Research: Oceans*, *125*(7), e2019JC015886. https://doi.org/10.1029/2019jc015886

Derakhti, M., Thomson, J., & Kirby, J. T. (2020). Sparse sampling of intermittent turbulence generated by breaking surface waves. *Journal of Physical Oceanography*, *50*(4), 867–885. https://doi.org/10.1175/jpo-d-19-0138.1

Donelan, M. A., Drennan, W. M., & Magnusson, A. K. (1996). Nonstationary analysis of the directional properties of propagating waves. *Journal of Physical Oceanography*, *26*(9), 1901–1914. https://doi.org/10.1175/1520-0485(1996)026<1901:NAOTDP>2.0.CO;2

Donelan, M. A., Hamilton, J., & Hui, W. (1985). Directional spectra of wind-generated ocean waves. *Proceedings of the Royal Society A: Mathematical, Physical & Engineering Sciences*, *315*(1534), 509–562.

Donelan, M. A., Haus, B. K., Plant, W. J., & Troianowski, O. (2010). Modulation of short wind waves by long waves. *Journal of Geophysical Research: Oceans*, *115*(C10). https://doi.org/10.1029/2009jc005794

Donelan, M. A., Longuet-Higgins, M. S., & Turner, J. S. (1972). Periodicity in whitecaps. *Nature*, *239*(5373), 449–451. https://doi.org/10.1038/239449a0

Dulov, V. A., Korinenko, A. E., Kudryavtsev, V. N., & Malinovsky, V. V. (2021). Modulation of wind-wave breaking by long surface waves. *Remote Sensing*, *13*(14), 2825. https://doi.org/10.3390/rs13142825

Dulov, V. A., Kudryavtsev, V. N., & Bol'shakov, A. N. (2002). A field study of whitecap coverage and its modulations by energy containing surface waves. In M. A. Donelan, W. M. Drennan, E. S. Saltzman, & R. Wanninkhof, (Eds.), *Gas transfer at water surfaces* (Vol. 127, pp. 187–192). American Geophysical Union.

Dysthe, K., Krogstad, H. E., & Müller, P. (2008). Oceanic rogue waves. *Annual Review of Fluid Mechanics*, *40*(1), 287–310. https://doi.org/10.1146/annurev.fluid.40.111406.102203

Fairall, C. W., Bradley, E. F., Hare, J. E., Grachev, A. A., & Edson, J. B. (2003). Bulk parameterization of air–sea fluxes: Updates and verification for the COARE algorithm. *Journal of Climate*, *16*(4), 571–591. https://doi.org/10.1175/1520-0442(2003)016<0571:BPOASF>2.0.CO;2

Fedele, F., Brennan, J., De León, S. P., Dudley, J., & Dias, F. (2016). Real world ocean rogue waves explained without the modulational instability. *Scientific Reports*, *6*, 27715. https://doi.org/10.1038/srep27715

Funke, E. R., & Mansard, E. P. D. (1980). On the synthesis of realistic sea states. *Coastal Engineering*, *1980*, 2974–2991. https://doi.org/10.1061/9780872622647.179

Furevik, B. R., & Haakenstad, H. (2012). Near-surface marine wind profiles from rawinsonde and NORA10 hindcast. *Journal of Geophysical Research: Atmospheres*, *117*(D23). https://doi.org/10.1029/2012jd018523

Gemmrich, J. R., & Farmer, D. M. (1999). Observations of the scale and occurrence of breaking surface waves. *Journal of Physical Oceanography*, *29*(10), 2595–2606. https://doi.org/10.1175/1520-0485(1999)029<2595:ootsao>2.0.co;2

Goda, Y. (1970). Numerical experiments on wave statistics with spectral simulation. *Report of the Port and Harbour Research Institute*, *9*, 3–57.

Guimaraes, P. V. (2018). *Sea surface and energy dissipation* (Unpublished doctoral dissertation). Université Bretagne Loire; École Centrale de Nantes.

Hasselmann, K. F., Barnett, T. P., Bouws, E., Carlson, H., Cartwright, D. E., Enke, K., et al. (1973). Measurements of wind-wave growth and swell decay during the joint North Sea wave project (JONSWAP). *Ergaenzungsheft zur Deutschen Hydrographischen Zeitschrift Reihe*, *A8*(12), 95.

Herbers, T. H. C., Jessen, P. F., Janssen, T. T., Colbert, D. B., & MacMahan, J. H. (2012). Observing ocean surface waves with GPS-tracked buoys. *Journal of Atmospheric and Oceanic Technology*, *29*(7), 944–959. https://doi.org/10.1175/jtech-d-11-00128.1

Holthuijsen, L. H. (2007). *Waves in oceanic and coastal waters*. Cambridge University Press.

Holthuijsen, L. H., & Herbers, T. H. C. (1986). Statistics of breaking waves observed as whitecaps in the open sea. *Journal of Physical Oceanography*, *16*(2), 290–297. https://doi.org/10.1175/1520-0485(1986)016<0290:sobwoa>2.0.co;2

Huang, K. Y., Katul, G. G., & Hultmark, M. (2021). Velocity and temperature dissimilarity in the surface layer uncovered by the telegraph approximation. *Boundary-Layer Meteorology*, *1–21*. https://doi.org/10.1007/s10546-021-00632-2

Huang, N. E., Shen, Z., & Long, S. R. (1999). A new view of nonlinear water waves: The Hilbert spectrum. *Annual Review of Fluid Mechanics*, *31*(1), 417–457. https://doi.org/10.1146/annurev.fluid.31.1.417

Huang, N. E., Shen, Z., Long, S. R., Wu, M. C., Shih, H. H., Zheng, Q., et al. (1998). The empirical mode decomposition and the Hilbert spectrum for nonlinear and non-stationary time series analysis. *Proceedings of the Royal Society A: Mathematical, Physical & Engineering Sciences*, *454*(1971), 903–995. https://doi.org/10.1098/rspa.1998.0193

Jähne, B., Klinke, J., & Waas, S. (1994). Imaging of short ocean wind waves: A critical theoretical review. *Journal of the Optical Society of America A*, *11*(8), 2197–2209.

Janssen, P. A. E. M., & Bidlot, J.-R. (2009). *On the extension of the freak wave warning system and its verification*. European Centre for Medium-Range Weather Forecasts.

Kara, A. B., Wallcraft, A. J., & Bourassa, M. A. (2008). Air-sea stability effects on the 10 m winds over the global ocean: Evaluations of air-sea flux algorithms. *Journal of Geophysical Research: Oceans*, *113*(C4). https://doi.org/10.1029/2007jc004324

Kimura, A. (1980). Statistical properties of random wave groups. *Coastal Engineering*, *1980*, 2955–2973. https://doi.org/10.1061/9780872622647.178

Kleiss, J. M., & Melville, W. K. (2010). Observations of wave breaking kinematics in fetch-limited seas. *Journal of Physical Oceanography*, *40*(12), 2575–2604. https://doi.org/10.1175/2010JPO4383.1

Kleiss, J. M., & Melville, W. K. (2011). The analysis of sea surface imagery for whitecap kinematics. *Journal of Atmospheric and Oceanic Technology*, *28*(2), 219–243. https://doi.org/10.1175/2010JTECHO744.1

Komen, G. J., Cavaleri, L., Donelan, M. A., Hasselmann, K., Hasselmann, S., & Janssen, P. A. E. M. (1994). *Dynamics and modelling of ocean waves*. Cambridge University Press.

Kudryavtsev, V., & Chapron, B. (2016). On growth rate of wind waves: Impact of short-scale breaking modulations. *Journal of Physical Oceanography*, *46*(1), 349–360.

Kuik, A. J., Van Vledder, G. P., & Holthuijsen, L. H. (1988). A method for the routine analysis of pitch-and-roll buoy wave data. *Journal of Physical Oceanography*, *18*(7), 1020–1034. https://doi.org/10.1175/1520-0485(1988)018<1020:AMFTRA>2.0.CO;2

Longuet-Higgins, M. S. (1975). On the joint distribution of the periods and amplitudes of sea waves. *Journal of Geophysical Research*, *80*(18), 2688–2694. https://doi.org/10.1029/jc080i018p02688

Longuet-Higgins, M. S. (1984). Statistical properties of wave groups in a random sea state. *Proceedings of the Royal Society A: Mathematical, Physical & Engineering Sciences*, *312*(1521), 219–250.

Longuet-Higgins, M. S., & Stewart, R. W. (1960). Changes in the form of short gravity waves on long waves and tidal currents. *Journal of Fluid Mechanics*, *8*(4), 565–583. https://doi.org/10.1017/S0022112060000803

Longuet-Higgins, M. S., & Stewart, R. W. (1964). Radiation stress in water waves: A physical discussion with application. *Deep-Sea Research*, *11*, 529–562. https://doi.org/10.1016/0011-7471(64)90001-4

Magnusson, A. K., & Donelan, M. A. (2013). The Andrea wave characteristics of a measured North Sea rogue wave. *Journal of Offshore Mechanics and Arctic Engineering*, *135*(3). https://doi.org/10.1115/1.4023800

Manaster, A., Ricciardulli, L., & Meissner, T. (2019). Validation of high ocean surface winds from satellites using oil platform anemometers. *Journal of Atmospheric and Oceanic Technology*, *36*(5), 803–818. https://doi.org/10.1175/jtech-d-18-0116.1

Melville, W. K. (1996). The role of surface-wave breaking in air-sea interaction. *Annual Review of Fluid Mechanics*, *28*(1), 279–321. https://doi.org/10.1146/annurev.fl.28.010196.001431

Michell, J. H. (1893). On the highest waves in water. *The London, Edinburgh, and Dublin Philosophical Magazine and Journal of Science*, *36*(222), 430–437. https://doi.org/10.1080/14786449308620499

Mironov, A. S., & Dulov, V. A. (2008). Detection of wave breaking using sea surface video records. *Measurement Science and Technology*, *19*(1), 015405. https://doi.org/10.1088/0957-0233/19/1/015405

Monahan, E. C., & O'Muircheartaigh, I. G. (1986). Whitecaps and the passive remote sensing of the ocean surface. *International Journal of Remote Sensing*, *7*(5), 627–642. https://doi.org/10.1080/01431168608954716

Monahan, E. C., & Woolf, D. K. (1989). Comments on "variations of whitecap coverage with wind stress and water temperature. *Journal of Physical Oceanography*, *19*(5), 706–709. https://doi.org/10.1175/1520-0485(1989)019<0706:COOWCW>2.0.CO;2

Paget, A. C., Bourassa, M. A., & Anguelova, M. D. (2015). Comparing in situ and satellite-based parameterizations of oceanic whitecaps. *Journal of Geophysical Research: Oceans*, *120*(4), 2826–2843. https://doi.org/10.1002/2014jc010328

Perlin, M., Choi, W., & Tian, Z. (2013). Breaking waves in deep and intermediate waters. *Annual Review of Fluid Mechanics*, *45*, 115–145. https://doi.org/10.1146/annurev-fluid-011212-140721

Phillips, O. M. (1985). Spectral and statistical properties of the equilibrium range in wind-generated gravity waves. *Journal of Fluid Mechanics*, *156*, 505–531. https://doi.org/10.1017/s0022112085002221

Reichert, K., Hessner, K., Nieto Borge, J. C., & Dittmer, J. (1999). WaMoS II: A radar based wave and current monitoring system. *Paper presented at the the ninth international offshore and polar engineering conference, Brest, France*.

Reul, N., Branger, H., & Giovanangeli, J.-P. (2008). Air flow structure over short-gravity breaking water waves. *Boundary-Layer Meteorology*, *126*(3), 477–505. https://doi.org/10.1007/s10546-007-9240-3

Romero, L. (2019). Distribution of surface wave breaking fronts. *Geophysical Research Letters*, *46*(17–18), 10463–10474. https://doi.org/10.1029/2019gl083408

Saket, A., Peirson, W. L., Banner, M. L., Barthelemy, X., & Allis, M. J. (2017). On the threshold for wave breaking of two-dimensional deep water wave groups in the absence and presence of wind. *Journal of Fluid Mechanics*, *811*, 642–658. https://doi.org/10.1017/jfm.2016.776

Salisbury, D. J., Anguelova, M. D., & Brooks, I. M. (2013). On the variability of whitecap fraction using satellite-based observations. *Journal of Geophysical Research: Oceans*, *118*(11), 6201–6222. https://doi.org/10.1002/2013jc008797

Scanlon, B., Breivik, Ø., Bidlot, J.-R., Janssen, P. A. E. M., Callaghan, A. H., & Ward, B. (2016). Modeling whitecap fraction with a wave model. *Journal of Physical Oceanography*, *46*, 887–894. https://doi.org/10.1175/JPO-D-15-0158.1

Scanlon, B., & Ward, B. (2013). Oceanic wave breaking coverage separation techniques for active and maturing whitecaps. *Methods in Oceanography*, *8*, 1–12. https://doi.org/10.1016/j.mio.2014.03.001

Scanlon, B., & Ward, B. (2016). The influence of environmental parameters on active and maturing oceanic whitecaps. *Journal of Geophysical Research: Oceans*, *121*(5), 3325–3336. https://doi.org/10.1002/2015jc011230

Schwendeman, M. S., & Thomson, J. (2015a). A horizon-tracking method for shipboard video stabilization and rectification. *Journal of Atmospheric and Oceanic Technology*, *32*(1), 164–176. https://doi.org/10.1175/jtech-d-14-00047.1

Schwendeman, M. S., & Thomson, J. (2015b). Observations of whitecap coverage and the relation to wind stress, wave slope, and turbulent dissipation. *Journal of Geophysical Research: Oceans*, *120*(12), 8346–8363. https://doi.org/10.1002/2015jc011196

Schwendeman, M. S., & Thomson, J. (2017). Sharp-crested breaking surface waves observed from a ship-based stereo video system. *Journal of Physical Oceanography*, *47*(4), 775–792. https://doi.org/10.1175/jpo-d-16-0187.1

Schwendeman, M. S., Thomson, J., & Gemmrich, J. R. (2014). Wave breaking dissipation in a young wind sea. *Journal of Physical Oceanography*, *44*(1), 104–127. https://doi.org/10.1175/jpo-d-12-0237.1

Smith, M. J., Poulter, E. M., & McGregor, J. A. (1996). Doppler radar measurements of wave groups and breaking waves. *Journal of Geophysical Research: Oceans*, *101*(C6), 14269–14282. https://doi.org/10.1029/96jc00766

Song, J.-B., & Banner, M. L. (2002). On determining the onset and strength of breaking for deep water waves. Part I: Unforced irrotational wave groups. *Journal of Physical Oceanography*, *32*(9), 2541–2558. https://doi.org/10.1175/1520-0485-32.9.2541

Sreenivasan, K. R., & Bershadskii, A. (2006). Clustering properties in turbulent signals. *Journal of Statistical Physics*, *125*(5), 1141–1153. https://doi.org/10.1007/s10955-006-9112-0

Stokes, G. G. (1880). *On the theory of oscillatory waves*. Transactions of the Cambridge Philosophical Society.

Sutherland, P., & Melville, W. K. (2015). Field measurements of surface and near-surface turbulence in the presence of breaking waves. *Journal of Physical Oceanography*, *45*(4), 943–965. https://doi.org/10.1175/jpo-d-14-0133.1

Terray, E. A., Donelan, M. A., Agrawal, Y. C., Drennan, W. M., Kahma, K. K., Williams, A. J., et al. (1996). Estimates of kinetic energy dissipation under breaking waves. *Journal of Physical Oceanography*, *26*(5), 792–807. https://doi.org/10.1175/1520-0485(1996)026<0792:EOKEDU>2.0.CO;2

Terrill, E., & Melville, W. K. (1997). Sound-speed measurements in the surface-wave layer. *Journal of the Acoustical Society of America*, *102*(5), 2607–2625. https://doi.org/10.1121/1.420315

Thomson, J. (2012). Wave breaking dissipation observed with "SWIFT" drifters. *Journal of Atmospheric and Oceanic Technology*, *29*(12), 1866–1882. https://doi.org/10.1175/JTECH-D-12-00018.1

Thomson, J., Gemmrich, J. R., & Jessup, A. T. (2009). Energy dissipation and the spectral distribution of whitecaps. *Geophysical Research Letters*, *36*(11). https://doi.org/10.1029/2009GL038201

Thomson, J., Schwendeman, M. S., Zippel, S. F., Moghimi, S., Gemmrich, J. R., & Rogers, W. E. (2016). Wave-breaking turbulence in the ocean surface layer. *Journal of Physical Oceanography*, *46*(6), 1857–1870. https://doi.org/10.1175/JPO-D-15-0130.1

Thorpe, S. (1982). On the clouds of bubbles formed by breaking wind-waves in deep water, and their role in air-sea gas transfer. *Philosophical Transactions of the Royal Society A*, *304*(1483), 155–210. https://doi.org/10.1098/rsta.1982.0011

Veltcheva, A., & Guedes Soares, C. (2007). Analysis of abnormal wave records by the Hilbert–Huang transform method. *Journal of Atmospheric and Oceanic Technology*, *24*(9), 1678–1689. https://doi.org/10.1175/JTECH2067.1

Veltcheva, A., & Guedes Soares, C. (2016). Analysis of wave groups by wave envelope-phase and the Hilbert Huang transform methods. *Applied Ocean Research*, *60*, 176–184. https://doi.org/10.1016/j.apor.2016.09.006

Yurovsky, Y. Y., Kudryavtsev, V. N., & Chapron, B. (2017). Simultaneous radar and video observations of the sea surface in field conditions. *Paper presented at the 2017 progress in electromagnetics research symposium-spring (piers)* (pp. 2559–2565). IEEE. https://doi.org/10.1109/piers.2017.8262183

Zappa, C. J., McGillis, W. R., Raymond, P. A., Edson, J. B., Hintsa, E. J., Zemmelink, H. J., & Ho, D. T. (2007). Environmental turbulent mixing controls on air-water gas exchange in marine and aquatic systems. *Geophysical Research Letters*, *34*(10). https://doi.org/10.1029/2006gl028790